



**HAL**  
open science

## Effect of deformation on helium storage and diffusion in polycrystalline forsterite

Rémi Delon, Sylvie Demouchy, Yves Marrocchi, Mohamed Ali Bouhifd, Julien Gasc, Patrick Cordier, Sanae Koizumi, Pete G Burnard

► **To cite this version:**

Rémi Delon, Sylvie Demouchy, Yves Marrocchi, Mohamed Ali Bouhifd, Julien Gasc, et al.. Effect of deformation on helium storage and diffusion in polycrystalline forsterite. *Geochimica et Cosmochimica Acta*, 2020, 273, pp.226-243. 10.1016/j.gca.2020.01.018 . hal-02951459

**HAL Id: hal-02951459**

**<https://hal.science/hal-02951459v1>**

Submitted on 30 Sep 2020

**HAL** is a multi-disciplinary open access archive for the deposit and dissemination of scientific research documents, whether they are published or not. The documents may come from teaching and research institutions in France or abroad, or from public or private research centers.

L'archive ouverte pluridisciplinaire **HAL**, est destinée au dépôt et à la diffusion de documents scientifiques de niveau recherche, publiés ou non, émanant des établissements d'enseignement et de recherche français ou étrangers, des laboratoires publics ou privés.

# Effect of deformation on helium storage and diffusion in polycrystalline forsterite

Rémi Delon<sup>1,\*</sup>, Sylvie Demouchy<sup>2</sup>, Yves Marrocchi<sup>1</sup>, Mohamed Ali Bouhifd<sup>3</sup>, Julien Gasc<sup>1,2</sup>,  
Patrick Cordier<sup>4</sup>, Sanae Koizumi<sup>5</sup> and Pete G. Burnard<sup>1</sup>

<sup>1</sup>Centre de recherches pétrographiques et géochimiques, UMR 7358, Université de Lorraine & CNRS, 15 rue Notre Dame des Pauvres, 54500 Vandoeuvre-lès-Nancy, France.

<sup>2</sup>Géosciences Montpellier, UMR 5243, Université de Montpellier & CNRS, Montpellier, France.

<sup>3</sup>Laboratoire Magmas et Volcans, UMR 6524, Université Clermont Auvergne & CNRS, Aubière, France.

<sup>4</sup>Univ. Lille, CNRS, INRA, ENSCL, UMR 8207 - UMET - Unité Matériaux et Transformations, F-59000 Lille, France

<sup>5</sup>Earthquake Research Institute, University of Tokyo, Tokyo, Japan

\* Corresponding author: remi.delon@uca.fr. Now at « Laboratoire Magmas et Volcans, UMR 6524, Université Clermont Auvergne & CNRS, 6 avenue Blaise Pascal, Aubière, France ».

Submitted to *Geochimica et Cosmochimica Acta* in May 2019

Revised for *Geochimica et Cosmochimica Acta* in January 2020

Accepted 11 january 2020, online 21 January 2020

1 *Abstract*

2 Although recent studies have investigated He behavior in undeformed mantle minerals, the  
3 effect of defects generated by plastic deformation on He storage and transport remains  
4 unconstrained. For this purpose, synthetic dense aggregates of fine-grained iron-free forsterite  
5 were deformed under 300 MPa confining pressure at 950, 1050, and 1200 °C using a Paterson  
6 press. Three deformed samples and one undeformed sample were then doped with He under  
7 static high-pressure ( $1.00 \pm 0.02$  GPa) and high-temperature ( $1120 \pm 20$  °C) conditions for 24  
8 h in a piston cylinder. Uraninite was used as a source of noble gases. The samples were  
9 subsequently analyzed using a cycled step heating protocol coupled with noble gas mass  
10 spectrometry to investigate He storage and diffusion in the deformed polycrystalline forsterite  
11 aggregates. Results show complex diffusive behaviors that cannot be fitted by a single linear  
12 regression. Nevertheless, individual step heating cycles can be fitted by several linear  
13 regressions determined by a *F*-test, suggesting that diffusivities follow Arrhenius law within  
14 the given temperature ranges. Our results highlight the complex diffusive behavior of He in  
15 deformed forsterite aggregates, which is due to the competition between several diffusion  
16 mechanisms related to different He storage sites (Mg vacancies, interstitial sites, dislocations,  
17 and grain boundaries). Diffusion parameters (activation energy  $E_a$  and pre-exponential factor  
18  $D_0$ ) for He diffusion in grain boundaries were refined from literature data ( $E_a = 36 \pm 9$  kJ·mol<sup>-1</sup>  
19 and  $D_0 = 10^{-10.57 \pm 0.58}$  m<sup>2</sup>·s<sup>-1</sup>), and those of He diffusion in interstitials ( $E_a = 89 \pm 7$  kJ·mol<sup>-1</sup>  
20 and  $D_0 = 10^{-8.95 \pm 1.16}$  m<sup>2</sup>·s<sup>-1</sup>) and Mg vacancies ( $E_a = 173 \pm 14$  kJ·mol<sup>-1</sup> and  $D_0 = 10^{-5.07 \pm 1.25}$   
21 m<sup>2</sup>·s<sup>-1</sup>) were defined from our results and literature data. Furthermore, we determined  $E_a = 56$   
22  $\pm 1$  kJ·mol<sup>-1</sup> and  $D_0 = 10^{-9.97 \pm 0.37}$  m<sup>2</sup>·s<sup>-1</sup> for He diffusion along dislocations. These results  
23 suggest that a maximum He fraction of only 1.2% can be stored along dislocations in mantle  
24 minerals, which is negligible compared to 22% in grain boundaries as reported by previous  
25 studies. This implies that bulk lattice diffusivities are barely affected by the presence of

26 dislocations, whereas the proportion of He stored in grain boundaries can significantly  
27 enhance the bulk diffusivities of mantle rocks. Thus, deformation processes can significantly  
28 increase He storage capacity by decreasing grain size (i.e., via dynamic recrystallization), but  
29 will not sufficiently increase the dislocation density to induce a change in He storage and  
30 mobility within the crystallographic lattice. Furthermore, rapid redistribution of He between  
31 the mineral lattice and grain boundaries could enhance the bulk He concentrations of  
32 deformed peridotites upon equilibration with nearby undeformed (or less-deformed)  
33 peridotites.

34

35 *Keywords:* helium, diffusion, storage, deformation, dislocation, forsterite

36

### 37 *1. Introduction*

38 The behavior of noble gases in the Earth's mantle provides important information and  
39 essential time constraints on chemical and isotopic mantle heterogeneities. Indeed, noble  
40 gases have both primordial and radiogenic isotopes and behave as both incompatible and  
41 volatile elements. Although they are not expected to be easily recycled during subduction  
42 processes (Moreira and Raquin, 2007; Staudacher and Allègre, 1988), several studies have  
43 reported evidences for noble gas recycling in the mantle (e.g., Holland and Ballentine, 2006;  
44 Parai and Mukhopahdyay, 2015; Kendrick et al., 2018; Smye et al., 2017). Nevertheless,  
45 differences in noble gas concentrations and isotopic ratios are still observed between mid-  
46 oceanic ridge basalts (MORBs) and ocean island basalts (OIBs), reflecting their different  
47 mantle sources (see Moreira, 2013, for a review). Helium (He) is a reliable tracer of mantle  
48 heterogeneities since its concentration is higher in MORBs than in OIBs (e.g., Moreira and  
49 Kurz, 2013), and the  $^3\text{He}/^4\text{He}$  ratio ( $R$ ) normalized to the atmospheric  $^3\text{He}/^4\text{He}$  ratio ( $R_a$ ) is  
50 homogeneous in MORBs (i.e.,  $R/R_a = 7-9$ ; e.g., Barfod et al., 1999), but varies from 4 (e.g.,

51 Farley et al., 1991; Moreira et al., 1999) up to almost 50 in OIBs (e.g., Hilton et al., 1997;  
52 Hiyagon et al., 1992; Honda et al., 1993; Kaneoka et al., 1983; Kurz et al., 1982, 1983; Rison  
53 and Craig, 1983; Starkey et al., 2009; Stuart et al., 2003; Valbracht et al., 1997). This  
54 dichotomy between MORBs and OIBs highlights the presence of at least two different  
55 sources in the Earth's mantle: (i) a primitive, less degassed source with low  $U/{}^3\text{He}$  and high  
56  $R/Ra$  ratios as the source of OIBs, and (ii) a more degassed source with higher  $U/{}^3\text{He}$  as the  
57 source of MORBs (e.g., Moreira and Kurz, 2013).

58 Although macroscopic models have been developed to explain the existence of these  
59 reservoirs by isolating the OIB source from mantle convection (Allègre, 1987; Bouhifd et al.,  
60 2013; Coltice et al., 2011; Labrosse et al., 2007; Porcelli and Halliday, 2001), the fundamental  
61 physical behavior of He in mantle minerals (e.g., storage sites, diffusion mechanisms)  
62 remained poorly understood despite recent improvements. Helium can be stored in various  
63 atomic defects within the crystal structure, such as 0-dimension defects (i.e., Mg vacancies  
64 and interstitial sites in olivine; Delon et al., 2018), 1-dimension defects (dislocations), 2-  
65 dimensions defects (i.e., interfaces and grain boundaries; Baxter et al., 2007; Burnard et al.,  
66 2015; Delon et al., 2018), and 3-dimensions defects (i.e., inclusions; Trull and Kurz, 1993).  
67 The storage of He in multiple sites induces a complex diffusive behavior due to the  
68 competition between different diffusion mechanisms related to each storage site. This  
69 complex diffusive behavior is shown schematically in Figure 1 by considering site-specific  
70 diffusion rates depending on the relative degree of disorder of the crystalline structure in each  
71 site (i.e., faster diffusion in more disordered sites). Regarding 1-dimension defects, Piazzolo et  
72 al. (2016) showed using atom probe tomography that incompatible elements are preferentially  
73 stored along dislocations in zircon. Nevertheless, their transport along dislocations remains  
74 poorly constrained.

75 Ar storage and transport in deformed minerals has been investigated in  
76 thermochronological studies, which showed that bulk diffusivities increase with deformation,  
77 thus decreasing Ar retention and producing younger Ar-Ar ages (Dunlap and Kronenberg,  
78 2001; Heizler et al., 1997; Kramar et al., 2001; Mulch et al., 2002; Reddy et al., 1996, 1999,  
79 2001). Recent studies have reported abnormally high concentrations of Ar near crystal  
80 surfaces for several minerals including quartz and feldspar (Baxter et al., 2006; Clay et al.,  
81 2010; Kelley et al., 2008; Watson and Cherniak, 2003), olivine and pyroxene (Thomas et al.,  
82 2008; Watson et al., 2007), and plagioclase (Wartho et al., 2014). These high Ar  
83 concentrations imply very low diffusivities that have been interpreted as representative of Ar  
84 lattice diffusivities, although recent bulk degassing experiments suggest a surface effect (e.g.,  
85 Burnard et al., 2015; Cassata et al., 2011; Delon et al., 2019). Such surface effects in  
86 mechanically prepared samples are in agreement with the study of Pinilla et al. (2012), who  
87 showed that diffusivities observed in the near-surface are not representative of bulk  
88 diffusivities due to the effect of interface adsorption, trapping Ar in dislocations, voids, and  
89 channels.

90 Although these results confirm the storage of noble gases in 1-dimension defects,  
91 abnormally high surface concentrations of He have only been observed in apatite (Van Soest  
92 et al., 2011), and the behavior of He in deformed minerals remains unconstrained. In this  
93 study, synthetic fine-grained polycrystalline iron-free forsterite was deformed at different  
94 temperatures, then experimentally doped with He at high pressure and high temperature. We  
95 analyzed the samples by step heating experiments to investigate He storage sites and diffusion  
96 in mantle olivine.

97

## 98 2. *Materials and methods*

### 99 2.1. *Starting materials and deformation experiments*

100 Forsterite samples used in this study were synthesized at the Earthquake Research Institute  
101 (Tokyo, Japan) from synthetic nano-powder made from colloidal SiO<sub>2</sub> (30 nm grain size) and  
102 Mg(OH)<sub>2</sub> (50 nm grain size). The sintering procedure was previously described by Koizumi et  
103 al. (2010) and is briefly summarized here. The powders were dispersed and mixed by ball  
104 milling for one day at a rate of ~250 rpm using 10-mm nylon-covered balls with iron cores  
105 and high-purity ethanol as a solvent. The samples were then dried at ~60 °C while stirring.  
106 The resulting powder was calcinated using an alumina tube furnace at 960 °C for 3 hours  
107 under an oxygen flow to remove decomposed products (H<sub>2</sub>O and CO<sub>2</sub>). The samples were  
108 pulverized with an agate mortar and pelletized using tungsten carbide dies to obtain disc-  
109 shaped samples, which were wrapped in a rubber sleeve and evacuated with a rotary pump.  
110 The compacted samples were then dropped into a water-medium pressure vessel and cold-  
111 pressed at 200 MPa for 10 min to produce pellets. The pellets were placed on a platinum  
112 crucible or plate in an alumina tube furnace with a vacuum diffusion pump and sintered at  
113 1260 °C for 2–3 h. The sintering conditions were carefully selected to maximize densification  
114 and minimize grain growth. The final porosity of the pellets was well below 1 vol.% (for  
115 further details, see Koizumi et al., 2010). The final products contained a low proportion  
116 (<2%) of iron-free enstatite to buffer the silica activity, but this abundance is too low to  
117 significantly modify the bulk diffusivities obtained during the subsequent step heating  
118 experiments (see section 4.1).

119 After sintering, the four cylindrical samples (NF\_SM, NF\_1200-1, NF\_1050-1, and  
120 NF\_950-1) had diameters of 4.5–4.8 mm and lengths of 7.25–10.55 mm. Three of them  
121 (NF\_1200-1, NF\_1050-1, and NF\_950-1) were used in deformation experiments performed at  
122 Geosciences Montpellier (University of Montpellier, France) in a gas-medium high pressure-  
123 high temperature apparatus (Paterson press; Paterson, 1990; Thieme et al., 2018). These  
124 samples were fit into metal sleeves (NF\_1200-1, NF\_1050-1, and NF\_950-1 into nickel,

125 copper, and silver sleeves, respectively), placed between alumina and zirconia pistons  
126 (Demouchy et al., 2014; Mei and Kohlstedt, 2000), and the assembly was encapsulated in an  
127 iron jacket. Deformation experiments were performed under uniaxial compression in an  
128 isostatic Ar pressure of 300 MPa at temperatures of 1200, 1050, and 950 °C for NF\_1200-1,  
129 NF\_1050-1, and NF\_950-1, respectively. Mechanical data and texture characterizations are  
130 fully reported in Gasc et al. (2019). After the deformation experiments, the samples were  
131 hand-polished to remove the metal sleeve and cut with a slow speed saw into millimeter-sized  
132 cubes. A first part of the recovered deformed fine-grained forsterite was used as starting  
133 material for doping experiments at high pressure and high temperature, and a second part was  
134 prepared for scanning electron microscopy (SEM), electron backscattered diffraction (EBSD)  
135 and transmission electron microscope (TEM) analyses for post-deformational grain size  
136 quantification and textural and microstructural characterization.

137 SEM and EBSD analyses were performed at Geosciences Montpellier with a CamScan  
138 X500FE Crystal Probe (see Demouchy et al., 2012) equipped with an EBSD system. Sample  
139 sections were prepared using a standardized polishing protocol (e.g., Thieme et al., 2018) and  
140 a final polishing step was performed using colloidal silica on a vibrating plate to obtain a  
141 high-quality polish for EBSD observation. Operating conditions were 15–18 kV and 6 or 10  
142 nA (for exposure times of 48 and 24 ms, respectively) at a working distance of 24–25 mm  
143 under low vacuum conditions (5 Pa of gaseous nitrogen) to avoid charging on the sample.  
144 Samples were carbon-coated and surrounded by copper-carbon conductive tape for EBSD  
145 analyses. EBSD maps were acquired with a step size of 0.2 or 0.4  $\mu\text{m}$ , allowing the grain size  
146 distributions to be determined after data treatment (Demouchy et al., 2014; Gasc et al., 2019).

147 For TEM analyses, post-deformation pre-doped samples were doubly polished to obtain  
148 30- $\mu\text{m}$ -thick thin sections, and glued on a Cu grid before ion milling at 5 kV under a low  
149 beam angle of 15° to reach electron transparency. The resulting foils were carbon-coated and

150 observed in a FEI® Tecnai G2-20 twin microscope operating at 200 kV at Unité Matériaux et  
151 Transformations (University of Lille, France).

152

## 153 *2.2. Doping experiments*

154 The deformed (NF\_1200-1, NF\_1050-1, and NF\_950-1) and undeformed (NF\_SM)  
155 samples were doped at high pressure and high temperature in the presence of a  $^4\text{He}$  source  
156 following a similar protocol described in Burnard et al. (2015), which was developed to  
157 mimic sub-solidus mantle conditions at low to medium noble gas partial pressure. In this  
158 study, the  $^4\text{He}$  source was uraninite powder from Mistamisk, Canada (for details, see Kish and  
159 Cuney, 1981). Doping experiments were performed at the Laboratoire Magmas et Volcans  
160 (Université Clermont Auvergne, Aubière, France) in a 3/4" piston cylinder. The samples were  
161 hand-polished to fit in 9-mm-long Pt capsules with an outer diameter of 5 mm and an inner  
162 diameter of 4.5 mm. Each sample was placed in a Pt capsule and separated from the uraninite  
163 powder by two Pt discs to avoid contamination of the samples by the He source, and any  
164 empty space was filled with San Carlos olivine powder, as shown in Fig. 2. The capsule was  
165 then closed by welding two Pt lids at each end, loaded in a Pyrex cylinder with two MgO  
166 cylinders at each end, and surrounded by MgO powder. The assembly was slid into a graphite  
167 furnace and placed in a Pyrex cylinder and a NaCl sleeve to ensure efficient pressure  
168 transmission and inhibit the occurrence of water (Fig. 2). Temperature was controlled and  
169 monitored using a  $\text{W}_5\text{Re}/\text{W}_{26}\text{Re}$  thermocouple (C-type) at the base of the Pt capsule (Fig. 2).  
170 External calibrations show a temperature gradient of less than 20 °C along the Pt capsule. The  
171 samples were annealed at  $1120 \pm 20$  °C and  $1.00 \pm 0.02$  GPa for ~24 h, and were quenched at  
172 high pressure. This long annealing stage at  $T > 1100$  °C and 1 GPa ensures complete collapse  
173 of residual porosity (from hot press at 300 MPa), closing up potential open grain boundaries  
174 (from grain sliding, see Gasc et al., 2019) and providing further dense sintering. At 1100 °C

175 and after 24 h only, intracrystalline ductility features are expected to be preserved (Farla et,  
176 2011). After the doping experiments, the samples were extracted from the capsules and cut  
177 into millimeter-sized cubes. For each sample, a single cube from the core was carefully  
178 selected to ensure that residual uraninite was not present during the subsequent noble gas  
179 analyses. Experimental conditions are summarized in Table 1.

180

### 181 *2.3. Helium analyses*

182 Helium analyses were performed using a cycled step heating protocol coupled with noble  
183 gas mass spectrometry, as detailed in Delon et al. (2018). Samples were annealed at different  
184 temperature steps and the gas extracted during each heating step was analyzed to obtain the  
185 molar quantity of He released, which permits calculation of the fractional gas loss and thus of  
186 the diffusion coefficient ( $D$ ) as a function of the square of the radius of the diffusion domain  
187 ( $a$ ). The corresponding equations were modified from Crank (1975), Fechtig and Kalbitzer  
188 (1966), and McDougall and Harrison (1999), and are presented in detail in Delon et al.  
189 (2018). Since  $D$  is related to temperature ( $T$ ) by an Arrhenius equation,  $D = f(1/T)$  (or  $D/a^2$  if  
190  $a$  is unknown) permits to obtain (i) the activation energy ( $E_a$ ), and (ii) the pre-exponential  
191 factor ( $D_0$  or  $D_0/a^2$  if  $a$  is unknown). Although the equations used to determine  $D$  were  
192 developed considering a homogeneous initial concentration in the sample, Delon et al. (2018)  
193 have already redeveloped them for heterogeneous initial concentration profiles. They reported  
194 no major change in the resulting diffusion parameters (within the error bars). Thus, even if  
195 samples were only partially doped, it does not impact the diffusion parameters calculated in  
196 this study.

197 Step heating analyses were performed at the Centre de Recherches Pétrographiques et  
198 Géochimiques (CNRS, Université de Lorraine, Nancy, France) using a Helix MC mass  
199 spectrometer, which was calibrated using aliquots ( $\sim 0.3$  cc,  $\sim 1.57 \times 10^{-8}$  mol) of an in-house

200 He standard (for further details, see Matsuda et al., 2002). The  $^4\text{He}$  signal was collected on a  
201 Faraday cup coupled with a  $10^{11} \Omega$  amplifier. A standard analysis was performed between  
202 each sample analysis, and the analytical sensitivity was calculated and used to obtain the  
203 molar quantity of He extracted during each heating step. The external error determined from  
204 these sensitivities was less than 8%, which represents a maximum external error of  $\pm 0.04$  on  
205 the resulting  $\log(D/a^2)$  values. Samples were loaded into a filament furnace, which consists of  
206 four alumina-coated tungsten evaporation baskets welded to two nickel rods as described in  
207 Bekaert et al. (2018). The furnace was calibrated by the melting points of tin, aluminum,  
208 copper and nickel, and the calibration curve (temperature as a function of the current) was  
209 obtained by second-order polynomial regression on the melting points. Before sample  
210 loading, the filament was degassed at  $\sim 1600$  °C under high vacuum for 1 h to remove any  
211 adsorbed atmospheric gases. A blank analysis was performed at  $\sim 1400$  °C before sample  
212 introduction (releasing  $8.69 \times 10^{-15}$  mol of He), and a cold blank analysis was performed for  
213 each sample: the molar quantities extracted during cold blank analyses represented less than  
214 10% ( $\sim 2.90 \times 10^{-15}$  mol) of those extracted during each heating step. Because of high blank  
215 signals, sample NF\_1200-1 was degassed under vacuum for 1 h at 800 °C before the step  
216 heating experiments to remove any gas adsorbed onto the sample surface, which greatly  
217 improved the blank signals. During this degassing step, He was lost and not analyzed, which  
218 can modify the initial He concentration profile of the sample. Nevertheless, a change in the  
219 initial concentration profile does not modify the resulting diffusion parameters (Delon et al.,  
220 2018). At each heating step, the temperature was held for 30 min, and the extracted gas was  
221 purified and analyzed, background and blank corrections were performed. Step heating  
222 experiments were cycled, meaning that each sample underwent several step heating sequences  
223 (cycles). A cycle consists in increasing the temperature between two heating steps, whereas  
224 the temperature is decreased at the end of a cycle to perform a second cycle on the same

225 sample, and so on. This protocol is used in thermochronology to identify diffusion domains  
226 that are not replenished (e.g., Reiners and Farley, 1999; Reiners et al., 2004) and has proved  
227 efficient for characterizing He storage sites in polycrystalline olivine (Delon et al., 2018).  
228 Individual step sequences are presented in Table 1. At the end of the cycled step heating  
229 experiments, the samples were fused at above 2000 °C and the extracted gas was analyzed to  
230 determine the total amount of He stored in the corresponding sample, and to back-calculate  
231 the fractional gas loss during each temperature step.

232

### 233 3. Results

#### 234 3.1. Textures and microstructures

235 Representative SEM and TEM images of pre-doped samples are displayed in Fig. 3, and  
236 additional images are available in Gasc et al. (2019). The average grain sizes determined from  
237 EBSD maps are reported in Table 1 and only slightly decreased during the deformation  
238 experiments. Grain size variations are expected to be negligible during the doping  
239 experiments since the diffusion length of silicon is only 0.56 nm in dry olivine (Dohmen et  
240 al., 2002) and 47 nm in wet olivine (Costa and Chakraborty, 2008) at the conditions of the  
241 doping experiments (i.e., 1120 °C and 24 h). SEM images of the four pre-doped samples  
242 show granoblastic textures with equilibrated triple junctions (Fig. 3a–d). Grain boundaries are  
243 mostly straight in samples NF\_SM, NF\_950-1, and NF\_1050-1, whereas they are  
244 occasionally slightly curved in NF\_1200-1. All samples have low porosities. Porosity appears  
245 to be more important in samples deformed at low temperature because they show grain  
246 boundaries opened by sliding, which creates voids during the deformation experiments (Gasc  
247 et al., 2019). If preserved during annealing at 1GPa, these 3-dimensions defects can trap noble  
248 gases during doping experiments, and their release can significantly impact the calculated  
249 diffusivities obtained during the step heating experiments. However, no gaps and voids are

250 expected to subsist under 1 GPa (e.g., German, 2014). Furthermore, several grains in the  
251 deformed samples showed internal contrast variations, highlighting the formation of subgrain  
252 boundaries (i.e., walls of dislocations), demonstrating that intracrystalline ductile deformation  
253 occurred (Fig. 3b–d).

254 TEM images show microstructures typical of deformed samples (i.e., straight dislocations,  
255 few dislocation loops, sub grain boundaries, Fig. 3e–h). These microstructures are mainly  
256 heterogeneous and due to microplasticity. Rare nanobubbles were also observed, which could  
257 act as a trap for He during doping experiments. In summary, the deformation experiments  
258 successfully involve 1-, 2-, and 3-dimensions defects (i.e., dislocations, subgrains, grain  
259 boundaries, and nanobubbles, respectively). We calculated the dislocation density ( $\rho$  in  $\text{m}^{-2}$ ,  
260 i.e., total length of dislocations in a unit volume of a crystal) for each deformed sample using  
261 Ham’s (1961) method, which consists in drawing straight lines of cumulative length  $L$  in  
262 random directions on a TEM image and counting the number of dislocations ( $N$ ) intersecting  
263 these lines. Using the sample thickness  $e$  (i.e., ~200 nm), dislocation density is estimated as:

$$\rho = \frac{2N}{L \cdot e} \quad . \quad (1)$$

264 We applied this method for four TEM images for sample NF\_950-1, one for NF\_1050-1, and  
265 three for NF\_1200-1, which were selected as being characteristic of the samples. The results  
266 confirm high dislocation densities for each deformed sample with mean values of  $2.3 \pm 1.2 \times$   
267  $10^{13} \text{ m}^{-2}$  for NF\_950-1,  $8.1 \times 10^{13} \text{ m}^{-2}$  for NF\_1050-1, and  $5.8 \pm 1.5 \times 10^{13} \text{ m}^{-2}$  for NF\_1200-  
268 1.

269

### 270 *3.2. Helium diffusivity*

271 Helium diffusivities are reported in Fig. 4 and the detailed data treatment is provided in  
272 supplementary file. The results show diffusive behavior that does not follow a single  
273 Arrhenius law since abrupt changes in slope occur in each Arrhenius diagram. Thus, our data

274 cannot be fitted with only one linear regression, suggesting different diffusion mechanisms at  
275 different temperature ranges. The best fit of our data by one, two, or three linear regressions  
276 and the associated transition temperatures were determined using  $F$ -tests on each cycle.  
277 Further details and results of the  $F$ -tests are available in supplementary material. The  $F$ -test is  
278 used to compare two models, and if the resulting  $F$  value is greater than the critical  $F$  value  
279 (available in  $F$  tables), the model with the fewest parameters is rejected. Otherwise, we chose  
280 the simpler model with the fewest parameters to fit our data (e.g., Box, 1953; Chow, 1960;  
281 Hahs-Vaughn and Lomax, 2013). For each cycle, we performed a  $F$ -test between a single  
282 linear regression (model 1) and all possible fits with two linear regressions (model 2,  
283 excluding all linear regressions fitted with less than three data points as irrelevant). If model 1  
284 was rejected, we compared the best-fit model with two linear regressions to models with three  
285 linear regressions, and so on. In the case where several models resulted in rejecting the  
286 comparative model, we chose the model with the greatest  $F$  value as the comparative model in  
287 subsequent tests or as the best fit to our data.

288 The linear regressions resulting from the  $F$ -tests are plotted in Fig. 4. The resulting  
289 diffusion parameters ( $E_a$  and  $D_0$  as a function of  $a^2$ ) are reported in Table 2 and vary widely:  
290  $E_a$  varied from  $3 \pm 6$  to  $330 \pm 29$  kJ·mol<sup>-1</sup> and  $\log(D_0/a^2)$  ( $D_0$  in m<sup>2</sup>·s<sup>-1</sup> and  $a$  in m) from  $-9.44$   
291  $\pm 0.82$  to  $7.98 \pm 1.29$ . This variation suggests a complex behavior of He diffusion in  
292 polycrystalline forsterite, with competition between different diffusive processes. However,  
293 since models with several linear regressions can fit our data, we can reasonably assume that  
294 diffusivities follow Arrhenius equations over the temperature ranges determined from the  $F$ -  
295 tests. These results were obtained by excluding some data points (open symbols in Fig. 4) at  
296 very low temperature (one each for NF\_SM and NF\_950-1) and at very high temperature (one  
297 for NF\_950-1 and two for NF\_1050-1) because they were considered as being distinctly  
298 different from the trend described by the nearby points.

299

## 300 4. Discussion

### 301 4.1. Mechanisms of He diffusion

302 The results of the  $F$ -tests show that models with several linear regressions for each cycle  
303 are the most relevant to fit our data. Thus, He diffusivity in our samples is complex, arising  
304 via competition between different diffusion mechanisms. Several hypotheses may explain  
305 why the diffusivities do not follow a single Arrhenius law: (i) the presence of a multi-  
306 diffusion domain (e.g., Harrison and Lovera, 2014; Lovera, 1992; Lovera et al., 1989), (ii) a  
307 competition between intrinsic and extrinsic diffusion at the atomic scale (e.g., Chakraborty,  
308 1997, 2008; Dohmen, 2008; Dohmen and Chakraborty, 2007), or (iii) a contribution of  
309 different diffusion mechanisms related to different storage sites, as has been observed for  
310 hydrogen (Demouchy, 2010; Mackwell and Kohlstedt, 1990; Padrón-Navarta et al., 2014;  
311 Thoraval and Demouchy, 2014), He, and Ar diffusion in undeformed polycrystalline olivine  
312 (Burnard et al., 2015; Delon et al., 2018, 2019). Because  $E_a$  values vary among linear  
313 regressions and transition temperatures differ between samples and even cycles, we favor the  
314 third hypothesis (see also Delon et al., 2018).

315 To confirm this hypothesis, we compare the diffusion parameters calculated from this  
316 study ( $E_a$  and  $\log D_0$ ) to those obtained for the different diffusive mechanisms observed in  
317 Burnard et al. (2015) and Delon et al. (2018) in Fig. 5. To calculate  $\log D_0$ ,  $a$  was chosen as  
318 half the sample size during the step heating experiments (i.e., 1 mm in this study), as was  
319 previously demonstrated in Delon et al. (2018). We follow the same usage as Delon et al.  
320 (2018) with LAT-high referring to diffusion in Mg vacancies, LAT-low to diffusion in  
321 interstitial sites, LAT to diffusion in the crystal lattice (i.e.,  $\text{LAT} = \text{LAT-high} + \text{LAT-low}$ ),  
322 and GB to grain boundary diffusion; when bulk diffusion is controlled by diffusion in several  
323 storage sites (co-governance), the implicated diffusions are separated by the + sign. The

324 formalisms of these different diffusive mechanisms are displayed in Table 3. The above  
325 studies showed that He diffusion in polycrystalline olivine occurs via LAT-high, LAT-high +  
326 LAT-low, and LAT + GB mechanisms, and we show the mean values (and the standard  
327 deviations) over which those mechanisms were reported to occur in Fig. 5. Most of the  $E_a$  and  
328  $\log D_0$  values from this study plot within those ranges, suggesting that LAT-high, LAT-high +  
329 LAT-low, and LAT + GB mechanisms were also observed in our diffusion experiments.  
330 Thus, the apparent non-Arrhenian behavior is due to diffusion mechanisms related to different  
331 storage sites, and transitions occurred upon the depletion of He in a storage site.

332 However, some diffusion parameters obtained herein clearly differ from those of the  
333 LAT-high, LAT-high + LAT-low, and LAT + GB mechanisms. Some  $E_a$  values are below the  
334 LAT + GB range (i.e.,  $<11 \text{ kJ}\cdot\text{mol}^{-1}$ ); these values seem to agree with those reported by  
335 Burnard et al. (2015) for Ar surface diffusion in olivine. Although the species are different,  
336 comparison between He and Ar surface diffusion is relevant in terms of  $E_a$ , but not in terms of  
337  $D_0$ . Indeed, the  $E_a$  for He surface diffusion is expected to be lower than that for LAT + GB  
338 mechanisms since He is only retained by Van der Waals bonds (i.e., low-energy interactions)  
339 at the sample surface. Furthermore, a low  $E_a$  value and one consistent with LAT + GB  
340 diffusion were obtained at lower and higher temperatures, respectively, during the same cycle  
341 (NF\_1050-1, cycle 1, Figs. 4 and 5), demonstrating that this low  $E_a$  mechanism (surface  
342 diffusion) is distinct from the LAT + GB mechanisms, and not simply LAT + GB diffusion  
343 with an abnormally low  $E_a$ .

344 Two  $E_a$  values (NF\_SM, cycle 1, and NF\_950-1, cycle 2) are near the lower limit of the  
345 LAT-high range. Instead of interpreting these as the LAT-high mechanism, we rather propose  
346 that the corresponding linear regressions were influenced by both the LAT-high and the LAT-  
347 high + LAT-low mechanisms. Indeed, Delon et al. (2018) demonstrated that a single  
348 regression encompassing these two mechanisms induced  $E_a$  and  $\log D_0$  values between those

349 for the LAT-high and LAT-high + LAT-low mechanisms (as in Blard et al., 2008; Cherniak  
350 and Watson, 2012), whereas performing two linear regressions on the same data points (one at  
351 lower temperature and another at higher temperature) returns values in agreement with those  
352 of the separate LAT-high and LAT-high + LAT-low mechanisms. We tested this by  
353 reprocessing these data points using three linear regressions instead of two (detailed results  
354 are reported in Table 2). Although the two-linear regression models presented for these  
355 samples in Fig. 4 were not rejected by the  $F$ -tests, the models with three linear regressions  
356 seem more suitable since the reprocessed data show diffusion parameters consistent with the  
357 distinct ranges of LAT-high and LAT-high + LAT-low mechanisms.

358 Diffusion parameters calculated from cycle 4 of sample NF\_SM do not seem to correlate  
359 with data from previous studies. This cycle was characterized by an abrupt increase of He  
360 release, inducing first a high  $E_a$  ( $\sim 330 \text{ kJ}\cdot\text{mol}^{-1}$ ) then a moderate  $E_a$  ( $\sim 120 \text{ kJ}\cdot\text{mol}^{-1}$ ). A  
361 similar burst in noble gas release was observed for Ar in pyroxenes and occurs upon early  
362 partial melting of the sample (Cassata et al., 2011). However, early partial melting of olivine  
363 has never been reported below  $1100 \text{ }^\circ\text{C}$  (under a pressure of 1-atm, Jaoul et al., 1987).  
364 Alternatively, He trapped in 3-dimensions defects (i.e., pores, voids) could significantly  
365 increase the release of He (and thus the resulting diffusivities), especially at high temperature.  
366 Indeed, the high  $E_a$  reported by Trull and Kurz (1993) for He diffusion in olivine has been  
367 interpreted as an energy of remobilization of He trapped in melt inclusions (e.g., Blard et al.,  
368 2008; Cherniak and Watson, 2012; Tolstikhin et al., 2010), highlighting the high-temperature  
369 dependency of this release. Thus, a minor contribution of He trapped in pores can  
370 significantly increase the apparent He release at high temperature and thus the resulting  
371 diffusivities, as observed in the diffusivities obtained for cycle 4 of sample NF\_SM (Fig. 4).  
372 A similar event could also explain the abnormal  $E_a$  values obtained for sample NF\_1200-1;  
373 two values are well above the LAT-high range, and another obtained at the highest

374 temperature range is abnormally low and thus does not actually correspond to LAT-high +  
375 LAT-low mechanisms. Another possibility to explain these abnormal diffusion parameters is  
376 the presence of enstatite in our samples. Indeed, orthopyroxene is more Ar-retentive than  
377 olivine since Ar diffusivities in orthopyroxene are significantly smaller than those in olivine  
378 (e.g., for orthopyroxene, see Cassata et al., 2011; for olivine, see Futagami et al., 1993; Delon  
379 et al., 2019), and this difference decreases with increasing temperature: for Ar, at 400 °C,  
380  $\log D \sim -19.92$  in olivine and  $-30.03$  in orthopyroxene, whereas at 1200 °C,  $\log D \sim -12.93$   
381 and  $-14.40$  in olivine and orthopyroxene, respectively, with  $D$  in  $\text{m}^2 \cdot \text{s}^{-1}$ ). We note that similar  
382 diffusive behavior is expected for He in olivine and orthopyroxene, and thus a relatively small  
383 He release from enstatite is predicted at low temperature whereas enstatite can significantly  
384 contribute to the He release at high temperature, resulting in enhanced calculated diffusivities,  
385 as shown in Fig. 4. A final explanation to interpret these high activation energies could be the  
386 absence of iron in our samples compared to those in Delon et al. (2018). Indeed, the  
387 incorporation of iron was proposed to impact the strength of olivine and the incorporation of  
388 hydrogen in olivine at pressure below 1 GPa (Zhao et al., 2001, 2009). The substitution of Mg  
389 by  $\text{Fe}^{3+}$  should create additional vacancies and enhance transport properties such as ionic  
390 diffusion (Nakamura & Schmalzried, 1984). Thus, it should decrease the activation energy.  
391 Although some activation energies are higher in this study than in Delon et al. (2018) for  
392 diffusion in Mg-vacancies, this is not systematically true, suggesting that an increase in  
393 activation energy is not due to the absence of iron the crystal lattice. An explanation for the  
394 consistent absence of iron effect could be that the number of defects created by the  
395 substitution of magnesium by iron is too low to significantly modify the mean distance  
396 between two Mg-vacancies and thus, the activation energy.

397 A last set of diffusion parameters observed only in deformed samples (NF\_950-1,  
398 NF\_1050-1, and NF\_1200-1) remains unexplained. The values of these diffusion parameters

399 are similar among the three samples, with mean values of  $E_a = 56 \pm 1 \text{ kJ}\cdot\text{mol}^{-1}$  and  $\log D_0 = -$   
400  $9.97 \pm 0.37$  ( $D_0$  in  $\text{m}^2\cdot\text{s}^{-1}$ ). Although the pre-exponential factors are in the LAT-high + LAT-  
401 low range, the  $E_a$  values plot between the LAT-high + LAT-low and LAT + GB ranges. As  
402 these diffusion parameters occurred only in deformed samples, they are interpreted as  
403 corresponding to the combined contribution of lattice diffusion and diffusion along  
404 dislocations (LAT + DIS). Indeed, the  $E_a$  values suggest that the corresponding storage site is  
405 less retentive than the crystal lattice but more than grain boundaries, and are thus associated  
406 with dislocations that occur in deformed samples. To investigate the He amount stored along  
407 dislocations in our samples, the approximation that He extracted during heating steps, which  
408 expressed the LAT + DIS mechanisms, can be done. It yields that  $5.79 \times 10^{-13}$ ,  $1.86 \times 10^{-11}$ ,  
409 and  $1.99 \times 10^{-12}$  mol of He are stored along dislocations for NF\_950-1, NF\_1050-1, and  
410 NF\_1200-1, respectively. Nevertheless, since each sample was doped separately with  
411 different starting amount of He, it is difficult to determine if these amounts represent solely a  
412 difference in dislocation density or results also from the experimental run conditions. For  
413 these reasons, He storage as a function of the absolute density in dislocations in our samples  
414 will not be discussed any further.

415

#### 416 *4.2. Diffusion along dislocations*

417 Here, we extract the diffusivities along dislocations from the bulk diffusivities expressed  
418 in the LAT + DIS temperature range for deformed samples. Similar to grain boundary  
419 diffusion, bulk diffusivities resulting from the combined contribution of lattice diffusion and  
420 diffusion along dislocations can express three kinetic regimes (e.g., Harrison, 1961; Lee,  
421 1995): the A-regime is mainly controlled by diffusion in the crystal lattice, the C-regime is  
422 controlled only by diffusion along dislocations, and the B-regime is the intermediate case (for  
423 further details on these kinetic regimes applied to grain boundary diffusion, see Dohmen and

424 Milke, 2010; Joesten, 1991; Mishin and Herzig, 1995, 1999). These kinetic regimes evolve  
 425 with diffusion time from the type C to the type B and ultimately to the type A regime. Thus, it  
 426 is important to constrain which kinetic regime occurred in our diffusion experiments to  
 427 identify the diffusion mechanism controlling the bulk diffusivities. The A-regime occurs for  
 428 diffusion times ( $t$ ) significantly higher than the boundary time ( $t_d$ ), defined as:

$$t_d = \frac{l_d^2}{4D^{\text{LAT}}} \quad , \quad (2)$$

429 where  $l_d$  is the mean spacing between dislocations ( $l_d = \sqrt{1/\rho}$ ) and  $D^{\text{LAT}}$  the lattice diffusion  
 430 coefficient. In our samples,  $l_d = 209, 111, \text{ and } 131 \text{ nm}$  in NF\_950-1, NF\_1050-1, and  
 431 NF\_1200-1, respectively. At 400 °C (the lowest temperature step), these dislocation spacings  
 432 yield  $t_d = 78, 22, \text{ and } 31 \text{ s}$  for NF\_950-1, NF\_1050-1, and NF\_1200-1, respectively, by  
 433 considering the mean values of the lattice diffusion parameters obtained by Delon et al.  
 434 (2018) and herein for the LAT-high + LAT-low mechanisms. Thus,  $t_d$  is significantly shorter  
 435 than the extraction duration during a heating step (1800 s), which means that the A-regime  
 436 always occurred in the step heating experiments when the LAT + DIS mechanisms was  
 437 expressed. In the A-regime, the bulk diffusion coefficient  $D^{\text{bulk}}$  can be calculated as a function  
 438 of the diffusion coefficient along dislocations ( $D^{\text{DIS}}$ ) and the lattice diffusion coefficient as:

$$D^{\text{bulk}} = g \cdot D^{\text{DIS}} + (1 - g) \cdot D^{\text{LAT}} \quad , \quad (3)$$

439 where  $g$  is the fraction of the diffusing atoms that are located along dislocations. However,  
 440 this equation was first derived by Hart (1957), but was developed assuming an equilibrium  
 441 model in which the transfer of the diffusing species is in equilibrium at a local scale (Lee,  
 442 1995). Since our samples were partially doped, this assumption may not hold, and we will not  
 443 extract  $D^{\text{DIS}}$  using Eq. (3).

444 Although theory predicts that the A-regime is expressed during the step heating  
 445 experiments, the consistency of the  $E_a$  and  $\log(D_0)$  values expressed by the deformed samples  
 446 in the LAT + DIS temperature range suggests that diffusion is mainly controlled by a single

447 mechanism here, diffusion along dislocations. To verify this hypothesis, we compared the  
448 mean values of  $E_a$  and  $\log D_0$  expressed in the LAT + DIS temperature range with those of  
449 diffusion along grain boundaries, in interstitial sites and in Mg vacancies (Fig. 6). Grain  
450 boundary diffusion parameters are from Delon et al. (2018), obtained using the same method,  
451 except that we performed a linear regression on four data points (instead of five) because the  
452 lowest temperature diffusivity of their sample RDPC150 does not describe the same trend as  
453 the other diffusivities expressing grain boundary diffusion: this reprocessing of the two data  
454 sets (Delon et al., 2018 and this study) yields  $E_a = 36 \pm 9 \text{ kJ}\cdot\text{mol}^{-1}$  and  $\log D_0 = -10.57 \pm 0.58$ .  
455 For diffusion in interstitial sites and in Mg vacancies, we use the mean values of the diffusion  
456 parameters expressed in the LAT-high + LAT-low and LAT-high temperature ranges,  
457 respectively, from Delon et al. (2018) and herein, leading to  $E_a = 89 \pm 7 \text{ kJ}\cdot\text{mol}^{-1}$  and  $\log D_0 =$   
458  $-8.95 \pm 1.16$  for diffusion in interstitials and  $E_a = 173 \pm 14 \text{ kJ}\cdot\text{mol}^{-1}$  and  $\log D_0 = -5.07 \pm 1.25$   
459 for diffusion in Mg vacancies. The diffusion equations corresponding to each diffusion  
460 mechanism are displayed in Table 3. According to Fig. 6, the diffusivities expressed in the  
461 LAT + DIS temperature range are bracketed between grain boundary and lattice diffusivities  
462 for temperatures between 400 °C (i.e., below mantle temperatures) and 1400 °C (the highest-  
463 temperature boundary of the olivine stability field; e.g., Akaogi et al., 1989). Only at high  
464 temperature do Mg vacancy diffusivities exceed those of the other mechanisms. Thus, the  
465 diffusivities obtained in the LAT + DIS temperature range are characteristic of a diffusion  
466 mechanism in a storage site with a level of structure/disorder comprised between those of  
467 point defects (i.e., interstitials, Mg vacancies) and 2-dimensions defects (i.e., grain  
468 boundaries). Then, the logical possibility for this storage site is dislocations (1-dimension  
469 defects) in the deformed samples. We thus interpret the diffusion coefficients obtained in the  
470 LAT + DIS temperature ranges as representative of diffusion along dislocations with the  
471 mean diffusion parameters  $E_a = 56 \pm 1 \text{ kJ}\cdot\text{mol}^{-1}$  and  $\log D_0 = -9.97 \pm 0.37$ . The enhancement

472 of He diffusion along dislocations is very modest as shown by Figure 6, except at very low  
473 temperature (below ca. 600 °C). Dislocations are often considered to be short circuit diffusion  
474 paths. Indeed, a recent measurement of impurity diffusivity along a single dislocation in  
475 aluminum has demonstrated a diffusivity enhancement of almost three orders of magnitude as  
476 compared with bulk diffusion (Legros et al. 2008). However, the situation varies strongly  
477 from a system to another since in SrTiO<sub>3</sub>, Marrocchelli et al. (2015) report no significant pipe  
478 diffusion of oxide ions at dislocation cores. In olivine, little data are available. Wolfenstine  
479 (1990) has interpreted low temperature creep data in single crystal of dry olivine based on the  
480 role of pipe diffusion. Gérard and Jaoul (1989) found no enhancement of oxygen diffusion by  
481 dislocations in San Carlos olivine, however, Yurimoto et al. (1992) reported diffusivities  
482 along dislocations for oxygen 10<sup>4</sup> times faster than lattice diffusivities in forsterite. To date,  
483 no diffusivity data are available for the role of dislocations on silicon diffusion, which is  
484 expected to be the creep rate limiting species. Our measurements represent the first indication  
485 of the role of dislocations on impurity diffusion in forsterite with a small effect on He  
486 diffusion, except at very low temperatures.

487       Nevertheless, at high temperature, diffusion in Mg vacancies shows higher diffusivities  
488 than the other diffusion mechanisms, contrary to what is expected. Diffusion in Mg vacancies  
489 might be more affected by increased pressure than the other diffusion mechanisms. Although  
490 no pressure effect has been observed up to 2.7 GPa for He lattice diffusion in olivine  
491 (Cherniak and Watson, 2012), first-principles calculations predict an influence up to 14 GPa  
492 (Wang et al., 2015), resulting in decreased diffusivity with increasing pressure. These results  
493 are in agreement with changes in Ni and Mn diffusivities in olivine with increasing pressure  
494 reported by Holzapfel et al. (2007). Since the compressibility of polyhedra increases with  
495 their size in the olivine lattice (e.g., Andraut et al., 1995), a similar assumption can be made  
496 for He storage sites in the olivine lattice. Thus, Mg sites should be more affected by

497 compression than interstitial sites, implying a greater decrease of He diffusivities via Mg  
498 vacancies with increasing pressure than via interstitials.

499

### 500 *4.3. Implications for the Earth's upper mantle*

501 To assess the implications of He storage along dislocations within the olivine stability  
502 field (i.e., until 410 km depth; Akaogi et al., 1989; Katsura et al., 2004) and assuming that  
503 dislocation creep controls olivine plastic deformation in the entire upper mantle, we have  
504 calculated the amount of He stored in dislocations compared to that stored in the crystal  
505 lattice. This proportion ( $g$ ) can be defined as a function of the partition coefficient between  
506 dislocations and the lattice ( $K^{\text{dis/lat}}$ ) and the volume fraction of dislocations ( $v^{\text{DIS}}$ ) as  
507 demonstrated by Lee (1995):

$$g = \frac{K^{\text{dis/lat}} \cdot v^{\text{DIS}}}{(K^{\text{dis/lat}} - 1) \cdot v^{\text{DIS}} + 1} \quad (4)$$

508 Although  $K^{\text{dis/lat}}$  is not known, it must be greater than 1 since He is an incompatible element  
509 (e.g., Heber et al., 2007; Jackson et al., 2013) and less than  $10^5$  (the highest value of the He  
510 partition coefficient between a silicate melt and the olivine lattice, see Delon et al., 2018).  
511 Thus, to obtain the maximum fraction of He stored along dislocations, we chose the  
512 maximum value of  $10^5$  for  $K^{\text{dis/lat}}$ . The value of  $v^{\text{DIS}}$  can be determined from the dislocation  
513 density ( $\rho$ ), which is between  $10^{10}$  and  $10^{12} \text{ m}^{-2}$  in the deformed lithospheric mantle (e.g.,  
514 Gueguen and Darot, 1980; Wallis et al., 2019), and the radius of the dislocation core ( $r$ ) as  
515  $v^{\text{DIS}} = \rho \cdot \pi r^2$  (Lee, 1995). For lithospheric mantle conditions, the maximum fraction of He  
516 stored along dislocations can be calculated for  $\rho = 10^{12} \text{ m}^{-2}$ . This yields a maximum value of  
517  $g$  of 1.2% for  $r = 2 \text{ \AA}$  (e.g., Durinck et al., 2007; Mahendran et al., 2017), meaning that only a  
518 negligible fraction of He (<1.2%) can be stored along dislocations in the Earth's upper  
519 mantle.

520 Concerning diffusion, the maximum value of  $t_d$  is obtained from Eq. (2) by considering a  
521 temperature of 900 °C (a realistic minimum lithospheric mantle temperature) and a low  $\rho$   
522 value. However,  $\rho$  is only available in the literature for deformed peridotites with a minimum  
523 value of  $10^{10} \text{ m}^{-2}$  (e.g., Gueguen and Darot, 1980). Nevertheless, at 900 °C,  $t_d$  is greater than  
524 1 yr for  $\rho < 10^6 \text{ m}^{-2}$  and  $t_d > 1 \text{ kyr}$  for  $\rho < 10^3 \text{ m}^{-2}$ . Thus, we can conclude that at geological  
525 time scales, the A-regime (which is expressed for durations greater than  $t_d$ ) always prevails in  
526 the Earth's mantle. Equation (3) can then be used to estimate bulk diffusivities in mantle  
527 minerals as a function of  $\rho$  and  $K^{\text{dis/lat}}$ . The influence of  $K^{\text{dis/lat}}$  is reported in Fig. 7 for a  
528 maximum value of  $\rho$  of  $10^{12} \text{ m}^{-2}$ , and the influence of  $\rho$  on bulk diffusivities is shown in the  
529 supplementary material for a reasonable  $K^{\text{dis/lat}}$  value of  $10^4$ . Bulk diffusivities increase with  
530 both  $K^{\text{dis/lat}}$  and  $\rho$ , but even at the maximum value of  $\rho$  observed in natural deformed  
531 peridotite (i.e.,  $10^{12} \text{ m}^{-2}$ ),  $K^{\text{dis/lat}}$  must be greater than  $10^5$  to significantly increase bulk  
532 diffusivities relative to lattice diffusivities. Moreover, the difference between bulk and lattice  
533 diffusivities decreases with increasing temperature, suggesting that bulk diffusivities are  
534 similar to lattice diffusivities in deformed mantle minerals.

535 Furthermore, Delon et al. (2018) demonstrated that a significant amount of He can be  
536 stored in grain boundaries (~22% at a grain size of 1 mm), enhancing the bulk diffusivities of  
537 mantle rocks. These results are highly dependent on grain size, implying that mantle  
538 deformation could significantly modify both the He storage capacity and bulk He diffusivities  
539 by grain size sensitive processes such as dynamic recrystallization (e.g., Kurz et al., 2009;  
540 Recanati et al., 2012). Indeed Kurz et al., (2009) reports a striking increase of He  
541 concentration as a function of the textures (from protogranular to mylonite) in rocks from St  
542 Paul Archipelago. However, the resulting dislocation density is not high enough to influence  
543 the storage and diffusive behavior of He in the mineral lattice of mantle rocks. Thus, the  
544 potential grain size reductions induced by dynamic recrystallization could result in a

545 redistribution of He between the mineral lattice and the grain boundary network to preserve a  
546 segregation factor of around  $10^5$  between grain boundaries and crystal lattice (Baxter et al.,  
547 2007; Delon et al., 2018). Two processes could play a role in such a He redistribution: (i) the  
548 diffusion of He through the crystal lattice and (ii) the motion of He-rich dislocations toward  
549 grain boundaries. At 800 °C, the velocity of He in olivine by diffusion process is around 50  
550  $\text{nm}\cdot\text{s}^{-1}$ , significantly higher than the mobility of dislocations under stresses characteristic of  
551 deformed peridotites (i.e., stresses between 10 and 200 MPa; e.g., Gueguen and Darot, 1980),  
552 which is less than  $10 \text{ nm}\cdot\text{s}^{-1}$  (Idrissi et al., 2016). Therefore, diffusion is the dominant process  
553 redistributing He between the olivine lattice and grain boundaries during plastic deformation.  
554 This process is very efficient since grain boundaries are equilibrated with olivine lattice in  
555 less than 3 hours at 800 °C at a grain size of 1 mm.

556        Nevertheless, the potential increased storage capacity of grain boundary network induced  
557 by dynamic recrystallization and grain size reduction does not imply an increase of bulk  
558 concentration, but only a redistribution of He between grain boundaries and the crystal lattice  
559 with respect to the segregation factor. To increase bulk concentrations, a homogenization  
560 must occur between the concentrations in grain boundaries (and thus in the crystal lattice to  
561 preserve the segregation factor) of rocks affected by dynamic recrystallization and those of  
562 nearby undeformed peridotites. To test this hypothesis in upper mantle rocks, we refer to  
563 Recanati et al. (2012), who studied the He abundance in protomylonites from a mantle shear  
564 zone (Josephine Peridotite, Oregon, USA) considered to be the remnant of a back-arc basin  
565 (e.g., Harper, 1984) or a fore-arc setting (e.g., Kelemen and Dick, 1995). The authors  
566 observed an abnormally high He concentration in a sample with a reduced grain size ( $\sim 285$   
567  $\mu\text{m}$ ) compared to adjacent rocks (average grain size of  $710 \mu\text{m}$ ). They interpreted this high He  
568 concentration as resulting from a higher volume fraction of grain boundaries, suggesting that  
569 the sample was in equilibrium with coarser-grained peridotites (i.e., with similar He

570 concentrations in grain boundaries and the crystal lattice). To calculate the lattice ( $C^{LAT}$ ) and  
 571 grain boundary ( $C^{GB}$ ) concentrations in these two rocks of different grain size, we perform a  
 572 mass balance calculation by considering that the total He amount is equal to the combined  
 573 amount of He stored in the crystal lattice and in grain boundaries. Based on the segregation  
 574 factor between grain boundaries and the crystal lattice ( $s$ ), and the volume fraction of grain  
 575 boundaries ( $v^{GB}$ ), we obtain:

$$C^{LAT} = \frac{C^{bulk}}{1 + sv^{GB}} \quad . \quad (5)$$

576 The value of  $s$  is taken as  $10^5$ , as observed by Baxter et al. (2007) in diopside and suggested  
 577 by Delon et al. (2018) in olivine, and  $v^{GB} = 2.84 \delta/d$  with  $\delta = 0.75$  nm being the grain  
 578 boundary width and  $d$  the grain size of the sample (Hiraga and Kohlstedt, 2009). We obtain  
 579  $C^{LAT} = 1.69 \pm 0.40 \times 10^{-12}$  mol·g<sup>-1</sup> for protomylonites with a grain size of 710  $\mu$ m and  $C^{LAT} =$   
 580  $2.98 \pm 0.20 \times 10^{-12}$  mol·g<sup>-1</sup> for the sample with a grain size of 285  $\mu$ m (for respective  $C^{bulk}$   
 581 values of  $2.20 \pm 0.52 \times 10^{-12}$  and  $5.20 \pm 0.35 \times 10^{-12}$  mol·g<sup>-1</sup>). Thus, the crystal lattice of the  
 582 sample with a reduced grain size is enriched in He by almost a factor of two compared to the  
 583 other samples, suggesting that dynamic recrystallization followed by homogenization with  
 584 nearby rocks is not the sole mechanism responsible for the observed He enrichment. Even if  
 585 this process can enhance bulk concentrations, a value of  $s$  around  $10^6$  is required to observe  
 586 the increased concentration reported by Recanati et al. (2012). Instead, fluid percolation  
 587 coupled with deformation could better explain the observed He enrichment. Indeed, fluid  
 588 circulation is expected in back-arc basins and fore-arc settings, and it is reasonable to assume  
 589 that this circulation occurs preferentially in deformed zones where percolation is easier due to  
 590 the higher volume fraction of grain boundaries.

591

592 5. *Conclusions*

593 The diffusivities we obtained on three deformed samples and one undeformed sample  
594 allow new constraints on He storage and mobility in polycrystalline rocks.

595 • Diffusivities cannot be explained by a single linear regression, suggesting that they do not  
596 follow a single Arrhenius law in deformed polycrystalline forsterite. However, each step  
597 heating cycle can be fitted by several linear regressions depending on the temperature  
598 range (and constrained by a *F*-test), highlighting that diffusivities follow Arrhenius law  
599 over limited temperature ranges. Thus, the diffusive behavior of He in deformed  
600 polycrystalline forsterite is complex due to the competition of several diffusion  
601 mechanisms that are preferentially expressed in different temperature ranges. These  
602 different diffusion mechanisms are related to various storage sites since (i) the transitions  
603 between the temperature ranges where different diffusion mechanisms are expressed were  
604 different between cycles and samples, and (ii) the calculated  $E_a$  show large variations  
605 within individual cycles.

606 • By comparison with literature data, we identified different diffusion mechanisms that  
607 were expressed for each linear regression: (i) the LAT-high mechanism (i.e., diffusion in  
608 Mg vacancies), (ii) the LAT-high + LAT-low mechanisms (i.e., the co-governance of  
609 diffusion in Mg vacancies and interstitial sites), (iii) the LAT + GB (i.e., the co-  
610 governance of diffusion in the crystal lattice and along grain boundaries), and (iv) surface  
611 diffusion. Moreover, we observed a new diffusion mechanism in deformed forsterite,  
612 interpreted as the LAT + DIS mechanisms (i.e., the co-governance of diffusion in the  
613 crystal lattice and along dislocations).

614 • We have refined grain boundary diffusion parameters for He in polycrystalline olivine:  $E_a$   
615 =  $36 \pm 9 \text{ kJ}\cdot\text{mol}^{-1}$  and  $D_0 = 10^{-10.57 \pm 0.58} \text{ m}^2\cdot\text{s}^{-1}$ . Based on our results and literature data, we  
616 have refined those of He diffusion in Mg vacancies ( $E_a = 173 \pm 14 \text{ kJ}\cdot\text{mol}^{-1}$  and  $D_0 = 10^{-$   
617  $5.07 \pm 1.25} \text{ m}^2\cdot\text{s}^{-1}$ ) and in interstitial sites ( $E_a = 89 \pm 7 \text{ kJ}\cdot\text{mol}^{-1}$  and  $D_0 = 10^{-8.95 \pm 1.16} \text{ m}^2\cdot\text{s}^{-1}$ ).

618 Furthermore, we report  $E_a = 56 \pm 1 \text{ kJ}\cdot\text{mol}^{-1}$  and  $D_0 = 10^{-9.97 \pm 0.37} \text{ m}^2\cdot\text{s}^{-1}$  for He diffusion  
619 along dislocations.

620 • By applying these results to Earth's upper mantle, we showed that only a small fraction of  
621 He is stored along dislocations in the crystal lattice (<1.2%), which is negligible compared  
622 to the He fraction stored in grain boundaries (~22% for a grain size of 1 mm; Delon et al.,  
623 2018). Thus, the presence of He along dislocations does not strongly influence bulk  
624 diffusivities, which are very close to lattice diffusivities, and only the existence of a  
625 significant amount of He in grain boundaries could enhance the bulk diffusivities of  
626 mantle rocks. Nevertheless, potential grain size reduction induced by dynamic  
627 recrystallization would involve a redistribution of He between the crystal lattice and grain  
628 boundaries, which can increase bulk concentrations upon re-equilibration of grain  
629 boundaries in deformed rocks with those in nearby undeformed peridotites, thus  
630 enhancing bulk He diffusivities.

631

### 632 *Acknowledgements*

633 This paper is dedicated to the memory of Pete Burnard (1965-2015), as the initiator of this  
634 project, our priceless colleague, and friend. The authors thank L. Zimmermann for his help on  
635 He analyses and D.V. Bekaert and M.W. Broadley for advice and assistance on the furnace.  
636 We are also grateful to M. Laumonier for his contribution to the piston cylinder experiments,  
637 J. Charreau for help with the  $F$ -tests, F. Barou for his help with SEM-EBSD analyses, and C.  
638 Nevado and D. Delmas for providing high-quality thin sections for SEM and TEM analyses.  
639 The TEM and EBSD-SEM national facilities in Lille and Montpellier are both supported by  
640 the Institut National de Sciences de l'Univers (INSU) du Centre National de la Recherche  
641 Scientifique (CNRS, France). The EBSD-SEM facility in Montpellier and TEM facility in  
642 Lille are also supported by the Conseil Régional Occitanie and by the Conseil Régional

643 Hauts-de-France (France), respectively. This study was supported by the JSPS KAKENHI  
644 Grant Number JP18K03799 to S. K. and Earthquake Research Institute's cooperative research  
645 program, 2016-B-05. M.A. Bouhifd acknowledges the support of the Labex ClerVolc (this is  
646 laboratory of Excellence ClerVolc contribution number 385). This study was mainly financed  
647 by l'Agence Nationale de la Recherche through grant ANR INDIGO (ANR-14-CE33-0011).  
648 This is CRPG contribution n° 2703.

649

#### 650 *Research data*

651 Original data of this study are available in the supplementary file.

652

#### 653 *References*

654 Akaogi, M., Ito, E., and Navrotsky, A. (1989). Olivine-modified spinel-spinel transitions in  
655 the system  $Mg_2SiO_4$ - $Fe_2SiO_4$ : Calorimetric measurements, thermochemical calculation,  
656 and geophysical application. *Journal of Geophysical Research: Solid Earth*, **94**(B11),  
657 15671–15685.

658 Allègre, C. J. (1987). Isotope geodynamics. *Earth and Planetary Science Letters*, **86**(2–4),  
659 175–203.

660 Andrault, D., Bouhifd, M. A., Itie, J. P., and Richet, P. (1995). Compression and  
661 amorphization of  $(Mg, Fe)_2SiO_4$  olivines: an X-ray diffraction study up to 70 GPa.  
662 *Physics and Chemistry of Minerals*, **22**(2), 99–107.

663 Barfod, D. N., Ballentine, C. J., Halliday, A. N., and Fitton, J. G. (1999). Noble gases in the  
664 Cameroon line and the He, Ne, and Ar isotopic compositions of high  $\mu$  (HIMU) mantle.  
665 *Journal of Geophysical Research: Solid Earth*, **104**(B12), 29509–29527.

666 Baxter, E. F., Clay, P. L., Kelley, S. P., Watson, E. B., Cherniak, D. J., and Thomas, J. B.  
667 (2006). Two diffusive pathways for argon in quartz and feldspar. *Geochimica et*

668 *Cosmochimica Acta Supplement*, 70, A41–A41.

669 Baxter, E. F., Asimow, P. D., and Farley, K. A. (2007). Grain boundary partitioning of Ar and  
670 He. *Geochimica et Cosmochimica Acta*, 71(2), 434–451.  
671 <https://doi.org/10.1016/j.gca.2006.09.011>

672 Bekaert, D. V., Broadley, M. W., Delarue, F.,  
673 Avice, G., Robert, F., and Marty, B. (2018). Archean kerogen as a new tracer of  
674 atmospheric evolution: Implications for dating the widespread nature of early life.  
675 *Science Advances*, 4(2), eaar2091. <https://doi.org/10.1126/sciadv.aar2091>

676 Blard, P.-H., Puchol, N., and Farley, K. A. (2008). Constraints on the loss of matrix-sited  
677 helium during vacuum crushing of mafic phenocrysts. *Geochimica et Cosmochimica*  
678 *Acta*, 72, 3788–3803. <https://doi.org/10.1016/j.gca.2008.05.044>

679 Bouhifd, M. A., Jephcoat, A. P., Heber, V. S., and Kelley, S. P. (2013). Helium in Earth's  
680 early core. *Nature Geoscience*, 6(11), 982.

681 Box, G. E. P. (1953). Non-normality and tests on variances. *Biometrika*, 40(3/4), 318–335.

682 Burnard, P., Demouchy, S., Delon, R., Arnaud, N. O., Marrocchi, Y., Cordier, P., and Addad,  
683 A. (2015). The role of grain boundaries in the storage and transport of noble gases in the  
684 mantle. *Earth and Planetary Science Letters*, 430, 260–270.  
685 <https://doi.org/10.1016/j.epsl.2015.08.024>

686 Cassata, W. S., Renne, P. R., and Shuster, D. L. (2011). Argon diffusion in pyroxenes:  
687 Implications for thermochronometry and mantle degassing. *Earth and Planetary Science*  
688 *Letters*, 304(3–4), 407–416. <https://doi.org/10.1016/j.epsl.2011.02.019>

689 Chakraborty, S. (1997). Rates and mechanisms of Fe-Mg interdiffusion in olivine at 980–  
690 1300 C. *Journal of Geophysical Research: Solid Earth*, 102(B6), 12317–12331.

691 Chakraborty, S. (2008). Diffusion in Solid Silicates: A Tool to Track Timescales of Processes  
692 Comes of Age. *Annual Review of Earth and Planetary Sciences*, 36(1), 153–190.  
<https://doi.org/10.1146/annurev.earth.36.031207.124125>

693 Cherniak, D. J., and Watson, E. B. (2012). Diffusion of helium in olivine at 1atm and 2.7GPa.  
694 *Geochimica et Cosmochimica Acta*, 84, 269–279.  
695 <https://doi.org/10.1016/j.gca.2012.01.042>

696 Chow, G. C. (1960). Tests of equality between sets of coefficients in two linear regressions.  
697 *Econometrica: Journal of the Econometric Society*, 591–605.

698 Clay, P. L., Baxter, E. F., Cherniak, D. J., Kelley, S. P., Thomas, J. B., and Watson, E. B.  
699 (2010). Two diffusion pathways in quartz: a combined UV-laser and RBS study.  
700 *Geochimica et Cosmochimica Acta*, 74(20), 5906–5925.

701 Coltice, N., Moreira, M., Hernlund, J., and Labrosse, S. (2011). Crystallization of a basal  
702 magma ocean recorded by helium and neon. *Earth and Planetary Science Letters*,  
703 308(1), 193–199.

704 Costa, F., and Chakraborty, S. (2008). The effect of water on Si and O diffusion rates in  
705 olivine and implications for transport properties and processes in the upper mantle.  
706 *Physics of the Earth and Planetary Interiors*, 166(1–2), 11–29.

707 Crank, J. (1975). *The Mathematics of Diffusion: 2d Ed.* Clarendon Press.

708 Delon, R., Demouchy, S., Marrocchi, Y., Bouhifd, M. A., Barou, F., Cordier, P., Addad, A.,  
709 Burnard, P. G. (2018). Helium incorporation and diffusion in polycrystalline olivine.  
710 *Chemical Geology*, 488(1), 105–124. <https://doi.org/10.1016/j.chemgeo.2018.04.013>

711 Delon, R., Demouchy, S., Marrocchi, Y., Bouhifd, M. A., Cordier, P., Addad, A., and  
712 Burnard, P. G. (2019). Argon storage and diffusion in Earth’s upper mantle. *Geochimica  
713 et Cosmochimica Acta*. <https://doi.org/10.1016/j.gca.2019.03.007>

714 Demouchy, S. (2010). Diffusion of hydrogen in olivine grain boundaries and implications for  
715 the survival of water-rich zones in the Earth’s mantle. *Earth and Planetary Science  
716 Letters*, 295(1–2), 305–313. <https://doi.org/10.1016/j.epsl.2010.04.019>

717 Demouchy, S., Tommasi, A., Barou, F., Mainprice, D., and Cordier, P. (2012). Deformation

718 of olivine in torsion under hydrous conditions. *Physics of the Earth and Planetary*  
719 *Interiors*, 202, 56–70.

720 Demouchy, S., Mussi, A., Barou, F., Tommasi, A., and Cordier, P. (2014). Viscoplasticity of  
721 polycrystalline olivine experimentally deformed at high pressure and 900 C.  
722 *Tectonophysics*, 623, 123–135. Dohmen, R. (2008). A new experimental thin film  
723 approach to study mobility and partitioning of elements in grain boundaries: Fe-Mg  
724 exchange between olivines mediated by transport through an inert grain boundary.  
725 *American Mineralogist*, 93(5–6), 863–874. <https://doi.org/10.2138/am.2008.2671>

726 Dohmen, R., and Chakraborty, S. (2007). Fe–Mg diffusion in olivine II: point defect  
727 chemistry, change of diffusion mechanisms and a model for calculation of diffusion  
728 coefficients in natural olivine. *Physics and Chemistry of Minerals*, 34(6), 409–430.

729 Dohmen, R., and Milke, R. (2010). Diffusion in Polycrystalline Materials: Grain Boundaries,  
730 Mathematical Models, and Experimental Data. *Reviews in Mineralogy and*  
731 *Geochemistry*, 72(1), 921–970. <https://doi.org/10.2138/rmg.2010.72.21>

732 Dohmen, R., Chakraborty, S., and Becker, H. (2002). Si and O diffusion in olivine and  
733 implications for characterizing plastic flow in the mantle. *Geophysical Research Letters*,  
734 29(21), 21–26. Dunlap, W. J., and Kronenberg, A. (2001). Argon loss during deformation  
735 of micas: constraints from laboratory deformation experiments. *Contributions to*  
736 *Mineralogy and Petrology*, 141(2), 174–185.

737 Durinck, J., Carrez, P., and Cordier, P. (2007). Application of the Peierls-Nabarro model to  
738 dislocations in forsterite. *European Journal of Mineralogy*, 19(5), 631–639.

739 Farla, R.J.M., Kokkonen, H., Fitz Gerald, J.D., Barnhoorn, A., Faul, U.H., Jackson, I., 2010.  
740 Dislocation recovery in fine-grained polycrystalline olivine. *Phys Chem Minerals* 38,  
741 363–377.

742 Farley, K. A., Basu, A. R., and Nilsson, K. (1991). Geochemistry and isotopic composition of

743 Guadalupe Island lavas and ultramafic xenoliths. *Eos, Trans. Am. Geophys. Union,*  
744 *72(500), 2509–2517.*

745 Fechtig, H., and Kalbitzer, S. (1966). The diffusion of argon in potassium-bearing solids. In  
746 *Potassium argon dating* (pp. 68–107). Springer.

747 Futagami, T., Ozima, M., Nagal, S., and Aoki, Y. (1993). Experiments on thermal release of  
748 implanted noble gases from minerals and their implications for noble gases in lunar soil  
749 grains. *Geochimica et Cosmochimica Acta*, *57(13)*, 3177–3194.  
750 [https://doi.org/10.1016/0016-7037\(93\)90302-D](https://doi.org/10.1016/0016-7037(93)90302-D)

751 Gasc, J., Demouchy, S., Barou, F., Koizumi, S., and Cordier, P. (2019). Creep mechanisms in  
752 the lithospheric mantle inferred from deformation of iron-free forsterite aggregates at  
753 900–1200° C. *Tectonophysics*. <https://doi.org/10.1016/j.tecto.2019.04.009>

754 Gérard, O., and Jaoul, O. (1989) Oxygen diffusion in San Carlos olivine. *Journal of*  
755 *Geophysical Research*, *94(B4)*, 4119–4128. <https://doi.org/10.1029/JB094iB04p04119>.

756 German, R. (2014). *Sintering: from empirical observations to scientific principles*.  
757 Butterworth-Heinemann.

758 Gueguen, Y., and Darot, M. (1980). Microstructures and stresses in naturally deformed  
759 peridotites. In *Tectonic Stresses in the Alpine-Mediterranean Region* (pp. 159–172).  
760 Springer.

761 Hahs-Vaughn, D. L., and Lomax, R. G. (2013). *Statistical concepts: A second course*.  
762 Routledge.

763 Ham, R. K. (1961). The determination of dislocation densities in thin films. *Philosophical*  
764 *Magazine*, *6(69)*, 1183–1184.

765 Harper, G. D. (1984). The Josephine ophiolite, northwestern California. *Geological Society of*  
766 *America Bulletin*, *95(9)*, 1009–1026.

767 Harrison, L. G. (1961). Influence of dislocations on diffusion kinetics in solids with particular

768 reference to the alkali halides. *Transactions of the Faraday Society*, 57, 1191.  
769 <https://doi.org/10.1039/tf9615701191>

770 Harrison, T. M., and Lovera, O. M. (2014). The multi-diffusion domain model: past, present  
771 and future. *Geological Society, London, Special Publications*, 378(1), 91–106.

772 Hart, E. W. (1957). On the role of dislocations in bulk diffusion. *Acta Metallurgica*, 5(10),  
773 597. [https://doi.org/http://dx.doi.org/10.1016/0001-6160\(57\)90127-X](https://doi.org/http://dx.doi.org/10.1016/0001-6160(57)90127-X)

774 Heber, V. S., Brooker, R. A., Kelley, S. P., and Wood, B. J. (2007). Crystal–melt partitioning  
775 of noble gases (helium, neon, argon, krypton, and xenon) for olivine and clinopyroxene.  
776 *Geochimica et Cosmochimica Acta*, 71(4), 1041–1061.

777 Heizler, M. T., Ralser, S., and Karlstrom, K. E. (1997). Late Proterozoic (Grenville?)  
778 deformation in central New Mexico determined from single-crystal muscovite  
779  $^{40}\text{Ar}/^{39}\text{Ar}$  age spectra. *Precambrian Research*, 84(1–2), 1–15.

780 Hilton, D. R., McMurtry, G. M., and Kreulen, R. (1997). Evidence for extensive degassing of  
781 the Hawaiian mantle plume from helium-carbon relationships at Kilauea volcano.  
782 *Geophysical Research Letters*, 24(23), 3065–3068.

783 Hiraga, T., and Kohlstedt, D. L. (2009). Systematic distribution of incompatible elements in  
784 mantle peridotite: Importance of intra- and inter-granular melt-like components.  
785 *Contributions to Mineralogy and Petrology*, 158(2), 149–167.  
786 <https://doi.org/10.1007/s00410-009-0375-8>

787 Hiyagon, H., Ozima, M., Marty, B., Zashu, S., and Sakai, H. (1992). Noble gases in  
788 submarine glasses from mid-oceanic ridges and Loihi seamount: constraints on the early  
789 history of the Earth. *Geochimica et Cosmochimica Acta*, 56(3), 1301–1316.

790 Holland, G., & Ballentine, C. J. (2006). Seawater subduction controls the heavy noble gas  
791 composition of the mantle. *Nature*, 441(7090), 186.

792 Holzapel, C., Chakraborty, S., Rubie, D. C., and Frost, D. J. (2007). Effect of pressure on

793 Fe–Mg, Ni and Mn diffusion in  $(\text{Fe}_x\text{Mg}_{1-x})_2\text{SiO}_4$  olivine. *Physics of the Earth and*  
794 *Planetary Interiors*, 162(3–4), 186–198.

795 Honda, M., McDougall, I., Patterson, D. B., Doulgeris, A., and Clague, D. A. (1993). Noble  
796 gases in submarine pillow basalt glasses from Loihi and Kilauea, Hawaii: a solar  
797 component in the Earth. *Geochimica et Cosmochimica Acta*, 57(4), 859–874.

798 Hull, D., Bacon, D.J. (1989). Introduction to dislocation, International Series on Materials  
799 Science and Technology. *Pergamon press*, New York.

800 Idrissi, H., Bollinger, C., Boioli, F., Schryvers, D., and Cordier, P. (2016). Low-temperature  
801 plasticity of olivine revisited with in situ TEM nanomechanical testing. *Science*  
802 *Advances*, 2(3), e1501671.

803 Jackson, C. R. M., Parman, S. W., Kelley, S. P., and Cooper, R. F. (2013). Constraints on  
804 light noble gas partitioning at the conditions of spinel-peridotite melting. *Earth and*  
805 *Planetary Science Letters*, 384, 178–187.

806 Jaoul, O., Houlier, B., Cheraghmakani, M., Pichon, R., and Liebermann, R. C. (1987).  
807 Surface destabilization and laboratory-induced non-stoichiometry in San Carlos olivine.  
808 *Physics and Chemistry of Minerals*, 15(1), 41–53.

809 Joesten, R. (1991). Grain-boundary diffusion kinetics in silicate and oxide minerals. In  
810 *Diffusion, atomic ordering, and mass transport* (pp. 345–395). Springer.

811 Kaneoka, I., Takaoka, N., and Clague, D. A. (1983). Noble gas systematics for coexisting  
812 glass and olivine crystals in basalts and dunite xenoliths from Loihi Seamount. *Earth and*  
813 *Planetary Science Letters*, 66, 427–437.

814 Kelemen, P. B., and Dick, H. J. B. (1995). Focused melt flow and localized deformation in  
815 the upper mantle: Juxtaposition of replacive dunite and ductile shear zones in the  
816 Josephine peridotite, SW Oregon. *Journal of Geophysical Research: Solid Earth*,  
817 100(B1), 423–438.

818 Kelley, S., Baxter, E., Cherniak, D., Clay, P., Thomas, J., and Watson, E. (2008). Two  
819 diffusion mechanisms for Argon in K-feldspar? *Geochimica et Cosmochimica Acta*  
820 *Supplement* (Vol. 72).

821 Kendrick, M. A., Scambelluri, M., Hermann, J., & Padrón-Navarta, J. A. (2018). Halogens  
822 and noble gases in serpentinites and secondary peridotites: Implications for seawater  
823 subduction and the origin of mantle neon. *Geochimica et Cosmochimica Acta*, 235, 285–  
824 304. <https://doi.org/10.1016/j.gca.2018.03.024>

825 Kish, L., and Cuney, M. (1981). Uraninite-albite veins from the Mistamisk Valley of the  
826 Labrador Trough, Quebec. *Mineralogical Magazine*, 44(336), 471–483.

827 Koizumi, S., Hiraga, T., Tachibana, C., Tasaka, M., Miyazaki, T., Kobayashi, T., Takamasa,  
828 A., Ohashi, N., and Sano, S. (2010). Synthesis of highly dense and fine-grained  
829 aggregates of mantle composites by vacuum sintering of nano-sized mineral powders.  
830 *Physics and Chemistry of Minerals*, 37(8), 505–518. [https://doi.org/10.1007/s00269-009-](https://doi.org/10.1007/s00269-009-0350-y)  
831 0350-y

832 Kramar, N., Cosca, M. A., and Hunziker, J. C. (2001). Heterogeneous  $^{40}\text{Ar}^*$  distributions in  
833 naturally deformed muscovite: in situ UV-laser ablation evidence for microstructurally  
834 controlled intragrain diffusion. *Earth and Planetary Science Letters*, 192(3), 377–388.

835 Kurz, M.D., Jenkins, W.J., Hart, S.R. (1982). Helium isotopic systematics of oceanic islands  
836 and mantle heterogeneity. *Nature*, 297, 43–47.

837 Kurz, M. D., Jenkins, W. J., Hart, S. R., and Clague, D. (1983). Helium isotopic variations in  
838 volcanic rocks from Loihi Seamount and the Island of Hawaii. *Earth and Planetary*  
839 *Science Letters*, 66, 388–406.

840 Kurz, M. D., Warren, J. M., & Curtice, J. (2009). Mantle deformation and noble gases :  
841 Helium and neon in oceanic mylonites. *Chemical Geology*, 266(1–2), 10–18.  
842 <https://doi.org/10.1016/j.chemgeo.2008.12.018>

843 Labrosse, S., Hernlund, J. W., and Coltice, N. (2007). A crystallizing dense magma ocean at  
844 the base of the Earth's mantle. *Nature*, 450(7171), 866.

845 Lee, J. K. W. (1995). Multipath diffusion in geochronology. *Contributions to Mineralogy and*  
846 *Petrology*, 120(1), 60–82. <https://doi.org/10.1007/BF00311008>

847 Legros, M., Dehm, G., Artz, E. and Balk, T.J. (2008) Observation of giant diffusivity along  
848 dislocation cores. *Science*, 319, 1646-1649. <https://doi.org/10.1126/science.1151771>

849 Lovera, O. M. (1992). Computer programs to model  $^{40}\text{Ar}/^{39}\text{Ar}$  diffusion data from  
850 multidomain samples. *Computers and Geosciences*, 18(7), 789–813.

851 Lovera, O. M., Richter, F. M., and Harrison, T. M. (1989). The  $^{40}\text{Ar}/^{39}\text{Ar}$  thermochronometry  
852 for slowly cooled samples having a distribution of diffusion domain sizes. *Journal of*  
853 *Geophysical Research: Solid Earth*, 94(B12), 17917–17935.  
854 <https://doi.org/10.1029/JB094iB12p17917>

855 Mackwell, S. J., and Kohlstedt, D. L. (1990). Diffusion of hydrogen in olivine: implications  
856 for water in the mantle. *Journal of Geophysical Research: Solid Earth*, 95(B4), 5079–  
857 5088.

858 Mahendran, S., Carrez, P., Groh, S., and Cordier, P. (2017). Dislocation modelling in  
859  $\text{Mg}_2\text{SiO}_4$  forsterite: an atomic-scale study based on the THB1 potential. *Modelling and*  
860 *Simulation in Materials Science and Engineering*, 25(5), 54002.

861 Marrocchelli, D., Sun, L. and Yildiz, B. (2015) Dislocations in  $\text{SrTiO}_3$ : Easy To Reduce but  
862 Not so Fast for Oxygen Transport. *Journal of the American Chemical Society*, 137,  
863 4735-4748. Doi: 10.1021/ja513176u.

864 Matsuda, J., Matsumoto, T., Sumino, H., Nagao, K., Yamamoto, J., Miura, Y., Sano, Y.  
865 (2002). The  $^3\text{He}/^4\text{He}$  ratio of new internal He Standard of Japan (HESJ). *Geochemical*  
866 *Journal*, 36(2), 191–195. <https://doi.org/10.2343/geochemj.36.191>

867 McDougall, I., and Harrison, T. M. (1999). Geochronology and Thermochronology by the

868  $^{40}\text{Ar}/^{39}\text{Ar}$  Method.

869 Mei, S., and Kohlstedt, D. L. (2000). Influence of water on plastic deformation of olivine  
870 aggregates: 1. Diffusion creep regime. *Journal of Geophysical Research: Solid Earth*,  
871 *105*(B9), 21457–21469.

872 Mishin, Y., and Herzig, C. (1995). Diffusion in fine-grained materials: Theoretical aspects  
873 and experimental possibilities. *Nanostructured Materials*, *6*(5–8), 859–862.  
874 [https://doi.org/10.1016/0965-9773\(95\)00195-6](https://doi.org/10.1016/0965-9773(95)00195-6)

875 Mishin, Y., and Herzig, C. (1999). Grain boundary diffusion: recent progress and future  
876 research. *Materials Science and Engineering: A*, *260*(1–2), 55–71.  
877 [https://doi.org/10.1016/S0921-5093\(98\)00978-2](https://doi.org/10.1016/S0921-5093(98)00978-2)

878 Moreira, M. (2013). Noble gas constraints on the origin and evolution of Earth’s volatiles.  
879 *Geochemical Perspectives*, *2*(2), 229–230.

880 Moreira, M. A., and Kurz, M. D. (2013). Noble gases as tracers of mantle processes and  
881 magmatic degassing. In *The Noble Gases as Geochemical Tracers* (pp. 371–391).  
882 Springer.

883 Moreira, M., and Raquin, A. (2007). The origin of rare gases on Earth: The noble gas  
884 “subduction barrier” revisited. *Comptes Rendus Geoscience*, *339*(14), 937–945.

885 Moreira, M., Doucelance, R., Kurz, M. D., Dupré, B., and Allègre, C. J. (1999). Helium and  
886 lead isotope geochemistry of the Azores Archipelago. *Earth and Planetary Science*  
887 *Letters*, *169*(1), 189–205.

888 Mulch, A., Cosca, M., and Handy, M. (2002). In-situ UV-laser  
889  $^{40}\text{Ar}/^{39}\text{Ar}$  geochronology of a micaceous mylonite: an example of defect-enhanced  
890 argon loss. *Contributions to Mineralogy and Petrology*, *142*(6), 738–752.

890 Nakamura, A., & Schmalzried, H. (1984). On the  $\text{Fe}^{2+}$ – $\text{Mg}^{2+}$ -Interdiffusion in Olivine (II).  
891 *Berichte Der Bunsengesellschaft Für Physikalische Chemie*, *88*(2), 140–145.

892 Padrón-Navarta, J. A., Hermann, J., and O’Neill, H. S. C. (2014). Site-specific hydrogen

893 diffusion rates in forsterite. *Earth and Planetary Science Letters*, 392, 100–112.

894 Parai, R., & Mukhopadhyay, S. (2015). The evolution of MORB and plume mantle volatile  
895 budgets: Constraints from fission Xe isotopes in Southwest Indian Ridge basalts.  
896 *Geochemistry Geophysics Geosystems*, 16(1), 719–735.  
897 <https://doi.org/10.1002/2014GC005566>

898 Paterson, M. S. (1990). Rock deformation experimentation. *The Brittle-Ductile Transition in*  
899 *Rocks*, 187–194.

900 Piazzolo, S., La Fontaine, A., Trimby, P., Harley, S., Yang, L., Armstrong, R., and Cairney, J.  
901 M. (2016). Deformation-induced trace element redistribution in zircon revealed using  
902 atom probe tomography. *Nature Communications*, 7.

903 Pinilla, C., Davis, S. a., Scott, T. B., Allan, N. L., and Blundy, J. D. (2012). Interfacial storage  
904 of noble gases and other trace elements in magmatic systems. *Earth and Planetary*  
905 *Science Letters*, 319–320, 287–294. <https://doi.org/10.1016/j.epsl.2011.12.018>

906 Porcelli, D., and Halliday, A. N. (2001). The core as a possible source of mantle helium.  
907 *Earth and Planetary Science Letters*, 192(1), 45–56.

908 Recanati, A., Kurz, M. D., Warren, J. M., and Curtice, J. (2012). Helium distribution in a  
909 mantle shear zone from the Josephine Peridotite. *Earth and Planetary Science Letters*,  
910 359, 162–172.

911 Reddy, S. M., Kelley, S. P., and Wheeler, J. (1996). A  $^{40}\text{Ar}/^{39}\text{Ar}$  laser probe study of micas  
912 from the Sesia Zone, Italian Alps: implications for metamorphic and deformation  
913 histories. *Journal of Metamorphic Geology*, 14(4), 493–508.

914 Reddy, S. M., Potts, G. J., Kelley, S. P., and Arnaud, N. O. (1999). The effects of  
915 deformation-induced microstructures on intragrain  $^{40}\text{Ar}/^{39}\text{Ar}$  ages in potassium feldspar.  
916 *Geology*, 27(4), 363–366.

917 Reddy, S. M., Potts, G. J., and Kelley, S. P. (2001).  $^{40}\text{Ar}/^{39}\text{Ar}$  ages in deformed potassium

918 feldspar: evidence of microstructural control on Ar isotope systematics. *Contributions to*  
919 *Mineralogy and Petrology*, 141(2), 186–200. Reiners, P. W., and Farley, K. A. (1999).  
920 Helium diffusion and (U-Th)/He thermochronometry of titanite. *Geochimica et*  
921 *Cosmochimica Acta*, 63(22), 3845–3859.  
922 <https://doi.org/10.1180/minmag.1998.62A.2.318>

923 Reiners, P. W., Spell, T. L., Nicolescu, S., and Zanetti, K. A. (2004). Zircon (U-Th)/He  
924 thermochronometry: He diffusion and comparisons with  $^{40}\text{Ar}/^{39}\text{Ar}$  dating. *Geochimica*  
925 *et Cosmochimica Acta*, 68(8), 1857–1887. <https://doi.org/10.1016/j.gca.2003.10.021>

926 Rison, W., and Craig, H. (1983). Helium isotopes and mantle volatiles in Loihi Seamount and  
927 Hawaiian Island basalts and xenoliths. *Earth and Planetary Science Letters*, 66, 407–  
928 426.

929 Smye, A. J., Jackson, C. R. M., Konrad-Schmolke, M., Hesse, M. A., Parman, S. W., Shuster,  
930 D. L., and Ballentine, C. J. (2017). Noble gases recycled into the mantle through cold  
931 subduction zones. *Earth and Planetary Science Letters*, 471, 65–73.

932 Starkey, N. A., Stuart, F. M., Ellam, R. M., Fitton, J. G., Basu, S., & Larsen, L. M. (2009).  
933 Helium isotopes in early Iceland plume picrites: Constraints on the composition of high  
934  $^3\text{He}/^4\text{He}$  mantle. *Earth and Planetary Science Letters*, 277(1–2), 91–100.  
935 <https://doi.org/10.1016/j.epsl.2008.10.007>

936 Staudacher, T., and Allègre, C. J. (1988). Recycling of oceanic crust and sediments: the noble  
937 gas subduction barrier. *Earth and Planetary Science Letters*, 89(2), 173–183.

938 Stuart, F. M., Lass-Evans, S., Fitton, J. G., & Ellam, R. M. (2003). High  $^3\text{He}/^4\text{He}$  ratios in  
939 picritic basalts from Baffin Island and the role of a mixed reservoir in mantle plumes.  
940 *Nature*, 424(6944), 57–59.

941 Thieme, M., Demouchy, S., Mainprice, D., Barou, F., and Cordier, P. (2018). Stress evolution  
942 and associated microstructure during transient creep of olivine at 1000–1200° C. *Physics*

943 *of the Earth and Planetary Interiors*, 278, 34–46.

944 Thomas, J. B., Cherniak, D. J., and Watson, E. B. (2008). Lattice diffusion and solubility of  
945 argon in forsterite, enstatite, quartz and corundum. *Chemical Geology*, 253(1–2), 1–22.  
946 <https://doi.org/10.1016/j.chemgeo.2008.03.007>

947 Thoraval, C., and Demouchy, S. (2014). Numerical models of ionic diffusion in one and three  
948 dimensions: application to dehydration of mantle olivine. *Physics and Chemistry of*  
949 *Minerals*, 41(9), 709–723.

950 Tolstikhin, I., Kamensky, I., Tarakanov, S., Kramers, J., Pekala, M., Skiba, V., Gannibal, M.,  
951 Novikov, D. (2010). Noble gas isotope sites and mobility in mafic rocks and olivine.  
952 *Geochimica et Cosmochimica Acta*, 74(4), 1436–1447.  
953 <https://doi.org/10.1016/j.gca.2009.11.001>

954 Trull, T. W., and Kurz, M. D. (1993). Experimental measurements of <sup>3</sup>He and <sup>4</sup>He mobility in  
955 olivine and clinopyroxene at magmatic temperatures. *Geochimica et Cosmochimica*  
956 *Acta*, 57(6), 1313–1324. [https://doi.org/10.1016/0016-7037\(93\)90068-8](https://doi.org/10.1016/0016-7037(93)90068-8)

957 Valbracht, P. J., Staudacher, T., Malahoff, A., and Allègre, C. J. (1997). Noble gas  
958 systematics of deep rift zone glasses from Loihi Seamount, Hawaii. *Earth and Planetary*  
959 *Science Letters*, 150(3), 399–411.

960 Van Soest, M. C., Monteleone, B. D., Hodges, K. V, and Boyce, J. W. (2011). Laser depth  
961 profiling studies of helium diffusion in Durango fluorapatite. *Geochimica et*  
962 *Cosmochimica Acta*, 75(9), 2409–2419.

963 Wallis, D., Hansen, L. N., Tasaka, M., Kumamoto, K. M., Parsons, A. J., Lloyd, G. E.,  
964 Kohlstedt, A.J., Wilkinson, A. J. (2019). The impact of water on slip system activity in  
965 olivine and the formation of bimodal crystallographic preferred orientations. *Earth and*  
966 *Planetary Science Letters*, 508, 51–61.

967 Wang, K., Brodholt, J., and Lu, X. (2015). Helium diffusion in olivine based on first

- 968 principles calculations. *Geochimica et Cosmochimica Acta*, 156, 145–153.
- 969 Wartho, J.-A., Kelley, S. P., and Elphick, S. C. (2014). Ar diffusion and solubility  
970 measurements in plagioclases using the ultra-violet laser depth-profiling technique.  
971 *Geological Society, London, Special Publications*, 378(1), 137–154.
- 972 Watson, E. B., and Cherniak, D. J. (2003). Lattice diffusion of Ar in quartz, with constraints  
973 on Ar solubility and evidence of nanopores. *Geochimica et Cosmochimica Acta*, 67(11),  
974 2043–2062.
- 975 Watson, E. B., Thomas, J. B., and Cherniak, D. J. (2007). <sup>40</sup>Ar retention in the terrestrial  
976 planets. *Nature*, 449(7160), 299.
- 977 Wolfenstine, J. (1990) Effects of pipe diffusion on the creep behaviour of dry olivine.  
978 *Philosophical Magazine Letters*, 62, 233-238.  
979 <https://doi.org/10.1080/09500839008215128>
- 980 Yurimoto, H., Morioka, M. and Nagasawa, H. (1992) Oxygen self-diffusion along high  
981 diffusivity paths in forsterite. *Geochemical Journal*, 26, 181-188.  
982 <https://doi.org/10.2343/geochemj.26.181>
- 983 Zhao, Y. and-H., Ginsberg, S., & Kohlstedt, D. L. (2001). Experimental investigation on  
984 water solubility in olivine single crystal with different Fe content. *Acta Petrologica*  
985 *Sinica*, 17(1), 123–128.
- 986 Zhao, Y. H., Zimmerman, M. E., & Kohlstedt, D. L. (2009). Effect of iron content on the  
987 creep behavior of olivine: 1. Anhydrous conditions. *Earth and Planetary Science Letters*,  
988 287(1–2), 229–240. <https://doi.org/10.1016/j.epsl.2009.08.006>

989

990

991 *Figure captions*

992 Fig. 1. Schematic representation of diffusion mechanisms related to storage sites in  
993 polycrystalline rocks undergoing doping by diffusion (e.g., chemical flux). The kinetic regime  
994 represented here is the B-regime (following the classification of Harrison, 1961) to highlight  
995 the different diffusion rates related to each storage types (point defects, dislocations, grain  
996 boundaries). Dislocation forests are local entanglement of linear defects and dislocation cores  
997 are the distortion of the lattice (inducing an extra strain energy) around a dislocation (e.g.,  
998 Hull and Bacon, 1984). An indicative scale is the cube edge = 10 nm.

999

1000 Fig. 2. Experimental sample assembly for doping experiments in piston cylinder.

1001

1002 Fig. 3. SEM images of post-deformation pre-doping polycrystalline olivine (a) sample  
1003 NF\_SM, which is the starting material (b) sample NF\_1200-1, (c) sample NF\_1050-1, and (d)  
1004 sample NF\_950-1. TEM images of microstructures in post-deformation pre-doping  
1005 polycrystalline olivine (e) sample NF\_1200-1 and (f–g) sample NF\_950-1.

1006

1007 Fig. 4. Arrhenius diagrams of He diffusion coefficients obtained from step heating analyses of  
1008 (a) undeformed sample NF\_SM and deformed samples (b) NF\_950-1, (c) NF\_1050-1, and (d)  
1009 NF\_1200-1. Multiple linear regressions were performed on each heating cycle, and the best-  
1010 fit model for each cycle was selected based on the results of *F*-tests (see text and  
1011 supplementary material). Gray dotted lines are the exceptions to *F*-tests, which were  
1012 preferentially chosen to better fit the data (see text for more details). The numbers of the  
1013 regressions correspond to the labeled data points in Fig. 5.

1014

1015 Fig. 5. Compilation of (a) the logarithm of the pre-exponential factors and (b) the activation  
1016 energies for samples from this study. Results are compared with Ar surface diffusion

1017 (Burnard et al., 2015), bulk He diffusion when lattice and grain boundary diffusion are  
1018 expressed (LAT + GB; Burnard et al., 2015; Delon et al., 2018), bulk He lattice diffusion  
1019 where diffusion in interstitial sites and Mg vacancies are expressed (LAT-high + LAT-low;  
1020 Delon et al., 2018), and He diffusion in Mg vacancies (LAT-high; Delon et al., 2018). Grey  
1021 points indicate data for the corresponding cycles that were reprocessed using three linear  
1022 regressions instead of two (see text). The numbers of the data points correspond to the  
1023 numbered linear regressions shown in Fig. 4.

1024

1025 Fig. 6. Arrhenius diagram of He grain boundary diffusion (reprocessed from Delon et al.,  
1026 2018), diffusion in interstitial sites and Mg vacancies (data from this study and Delon et al.,  
1027 2018), and combined diffusion in the crystal lattice and along dislocations (i.e., LAT + DIS  
1028 mechanisms, this study).

1029

1030 Fig. 7. Bulk lattice diffusivities (black dotted lines) calculated from Eq. (3) as a function of  
1031 temperature for different values of  $K^{\text{dis/lat}}$  and the maximum value of  $\rho$  in the Earth's mantle  
1032 ( $10^{12} \text{ m}^{-2}$ ). Diffusion along dislocations (green line) and diffusion in interstitials (orange line)  
1033 are shown for comparison.

1034

1035 *Table captions*

1036 Table 1. Experimental conditions for deformation, doping, and step heating experiments.  
1037 Average grain sizes were determined from SEM-EBSD maps.

1038

1039 Table 2. He diffusion parameters,  $\log(D_0/a^2)$  and  $E_a$ , obtained from each linear regression,  
1040 which were defined using  $F$ -tests for each heating step cycle. Data from two cycles were

1041 reprocessed to fit the data using three linear regressions instead of two as we favored this  
1042 model instead of the results of the  $F$ -tests (see text for more details).

1043

1044 Table 3. Diffusion equations defining helium diffusion in polycrystalline olivine from this  
1045 study and Delon et al. (2018).

**Table**

Type of experiment	Temperature	Pressure	Duration	Strain	Sample	Mass	Average grain size
	°C	MPa		%		mg	µm
<i>Deformation experiments</i>							
Paterson Press	1200 ± 25	300 ± 10	3h03	10.0	NF_1200-1	–	3.1
Paterson Press	1050 ± 25	300 ± 10	3h31	10.4	NF_1050-1	–	2.9
Paterson Press	950 ± 25	300 ± 10	2h48	3.1	NF_950-1	–	2.7
<i>Doping experiments</i>							
Piston cylinder	1120 ± 20	1 000 ± 20	24 h	–	NF_SM	47	3.1
					Uraninite	16	–
Piston cylinder	1120 ± 20	1 000 ± 20	24 h	–	NF_1200-1	46	3.1
					Uraninite	11	–
Piston cylinder	1120 ± 20	1 000 ± 20	24 h	–	NF_1050-1	96	2.9
					Uraninite	10	–
Piston cylinder	1120 ± 20	1 000 ± 20	24 h	–	NF_950-1	69	2.7
					Uraninite	12	–
<i>Cycled step heating experiments</i>							
Helix MC	Every 50 or 100 °C	around 10 <sup>-12</sup>	30 min per step	–	NF_SM	9.3	3.1
	Cycle 1: 400-800 °C						
	Cycle 2: 600-650 °C						
	Cycle 3: 400-650 °C						
	Cycle 4: 650-1300 °C						
Helix MC	Every 50 or 100 °C	around 10 <sup>-12</sup>	30 min per step	–	NF_1200-1	8.0	3.1
	Cycle 1: 400-750 °C						
	Cycle 2: 500-1200 °C						
Helix MC	Every 50 or 100 °C	around 10 <sup>-12</sup>	30 min per step	–	NF_1050-1	8.8	2.9
	Cycle 1: 400-1100 °C						
	Cycle 2: 400-1000 °C						
Helix MC	Every 50 °C	around 10 <sup>-12</sup>	30 min per step	–	NF_950-1	3.6	2.7
	Cycle 1: 400-950 °C						
	Cycle 2: 400-1000 °C						

*Table 1*

Sample		Temperature range °C	Activation energy kJ.mol <sup>-1</sup>	Log( $D_0/a^2$ ) m <sup>2</sup> .s <sup>-1</sup> /m <sup>2</sup>	
NF_SM	<i>Cycle 1</i>	401–556	6 ± 12	-9.44 ± 0.82	
		602–805	146 ± 11	-0.89 ± 0.57	
	<i>Cycle 1 (reprocessed)</i>	401–509	2 ± 24	-9.70 ± 1.70	
		556–649	88 ± 8	-4.25 ± 0.47	
		695–805	173 ± 17	0.50 ± 0.87	
	<i>Cycle 2</i>	602–649	11	-8.22	
	<i>Cycle 3</i>	509–649	89 ± 10	-3.80 ± 0.58	
	<i>Cycle 4</i>	852–946	330 ± 29	7.98 ± 1.29	
		993–1295	120 ± 8	-1.01 ± 0.29	
	NF_950-1	<i>Cycle 1</i>	447–649	10 ± 7	-5.47 ± 0.42
695–946			89 ± 8	-1.45 ± 0.39	
<i>Cycle 2</i>		602–758	68 ± 6	-3.07 ± 0.36	
		805–946	150 ± 1	1.0 ± 0.01	
<i>Cycle 2 (reprocessed)</i>		602–695	56 ± 1	-3.76 ± 0.02	
		695–805	96 ± 3	-1.63 ± 0.17	
		852–946	150 ± 1	1.00 ± 0.03	
NF_1050-2		<i>Cycle 1</i>	401–602	3 ± 6	-5.52 ± 0.42
			649–805	22 ± 5	-4.64 ± 0.22
			852–993	77 ± 4	-1.82 ± 0.15
	<i>Cycle 2</i>	401–494	20 ± 16	-6.04 ± 1.18	
		556–993	55 ± 2	-3.76 ± 0.13	
	NF_1200-1	<i>Cycle 1</i>	401–602	100 ± 6	-2.96 ± 0.41
649–758			228 ± 1	4.45 ± 0.02	
<i>Cycle 2</i>		494–649	57 ± 2	-4.40 ± 0.14	
		695–805	201 ± 2	3.29 ± 0.12	
		899–1199	88 ± 1	-1.89 ± 0.06	

N.B. Activation energies are calculated with  $a = 1$  m as activation energies do not depend on the value of  $a$  (see Burnard *et al.*, 2015 for further details)

*Table 2*

Diffusion mechanism	Formal notations	Diffusion equation	References
Diffusion via Mg vacancies	LAT-high	$D = 10^{-5.07 \pm 1.25} \exp [-(173,000 \pm 14,000)/RT]$	Delon et al., 2018 This study
Diffusion via interstitials	LAT-low	$D = 10^{-8.95 \pm 1.16} \exp [-(89,000 \pm 7,000)/RT]$	Delon et al., 2018 This study
Diffusion along dislocations	DIS	$D = 10^{-9.97 \pm 0.37} \exp [-(56,000 \pm 1,000)/RT]$	This study
Diffusion via grain boundaries	GB	$D = 10^{-10.57 \pm 0.58} \exp [-(36,000 \pm 9,000)/RT]$	Delon et al., 2018

*Table 3*

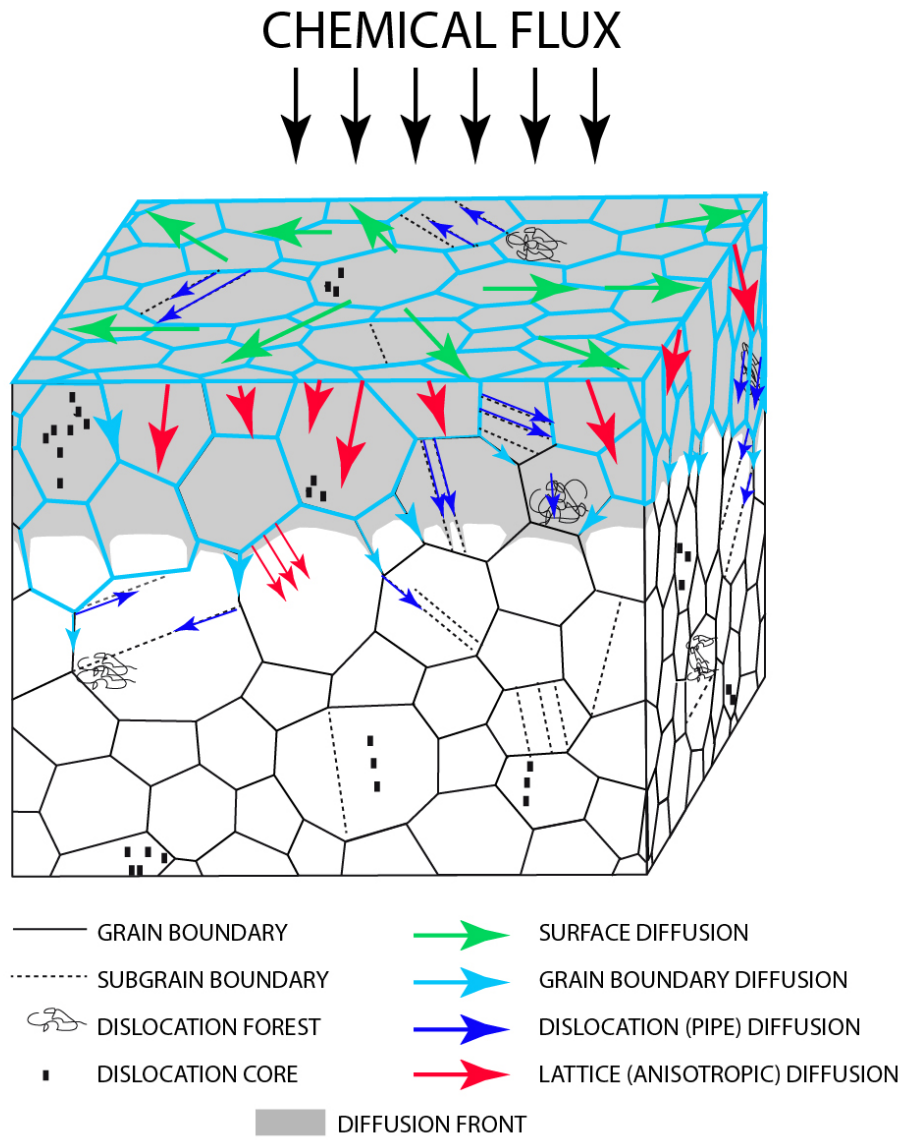


*Figure 1*

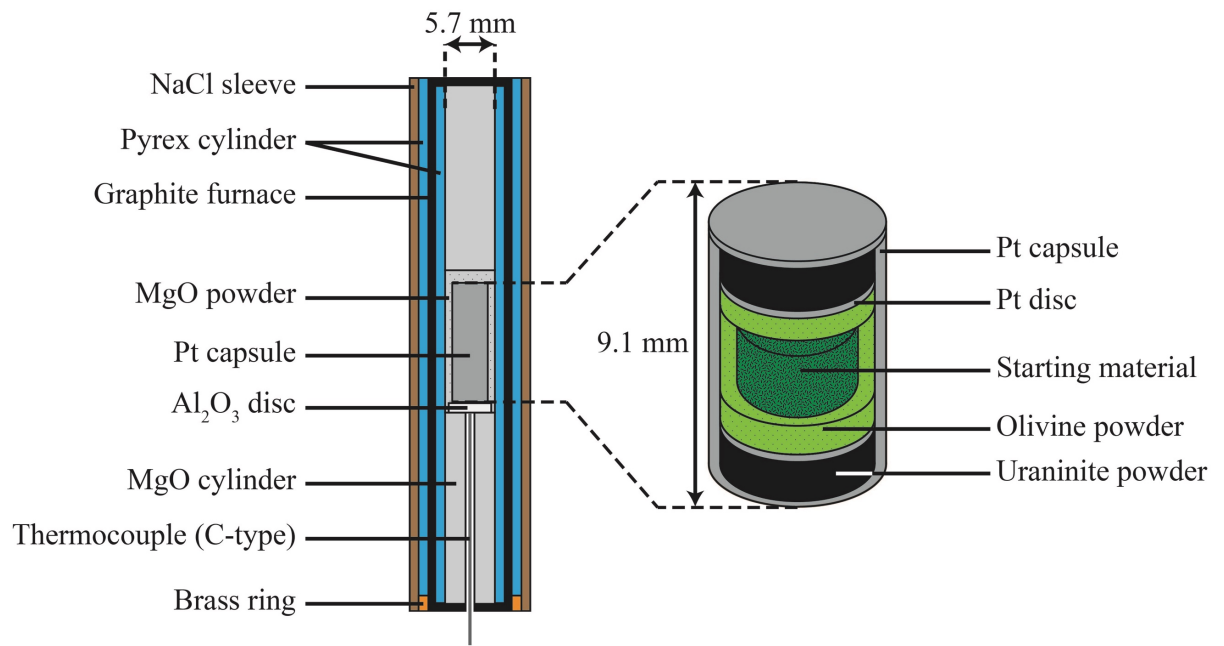


*Figure 2*

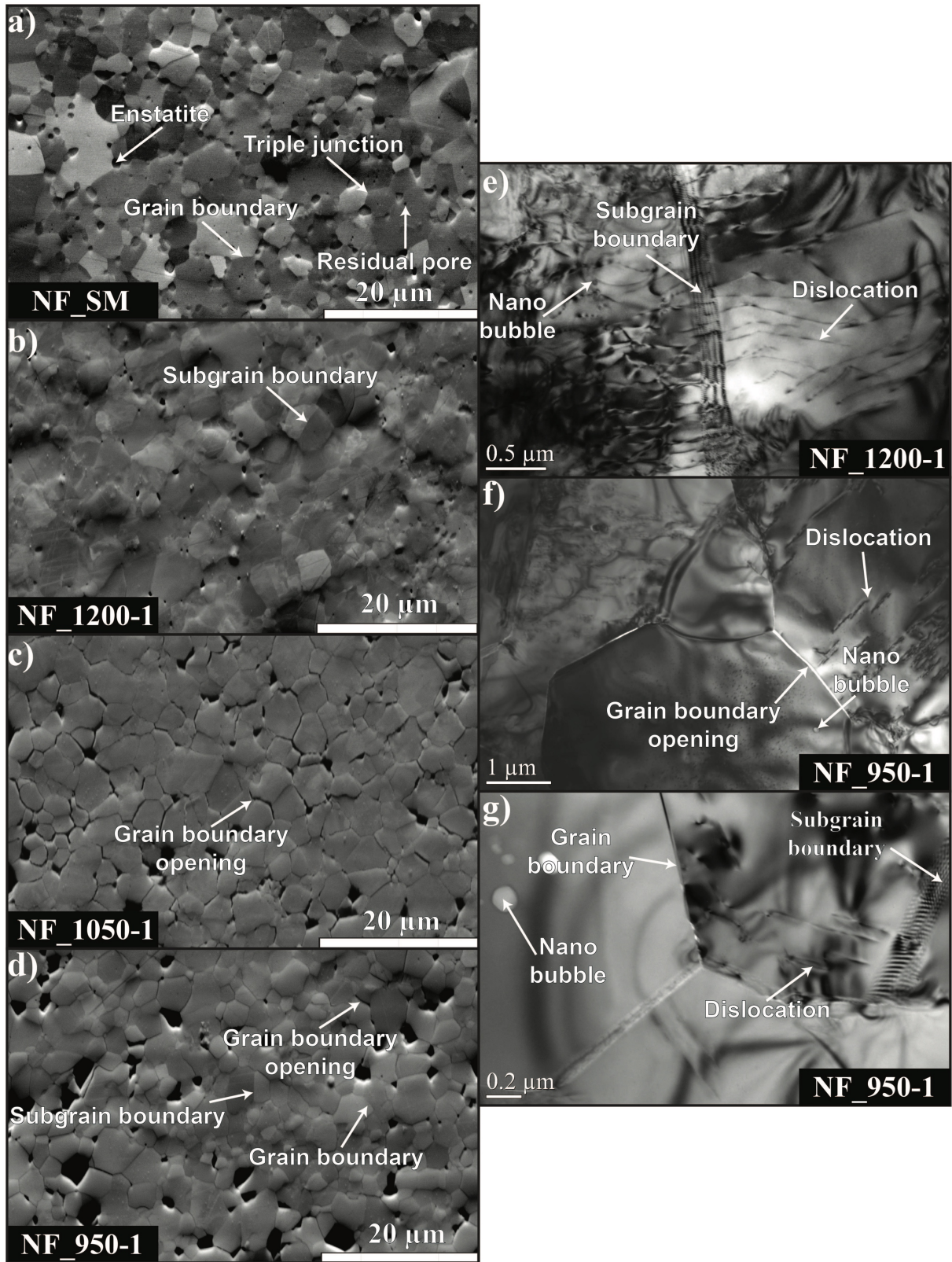


Figure 3

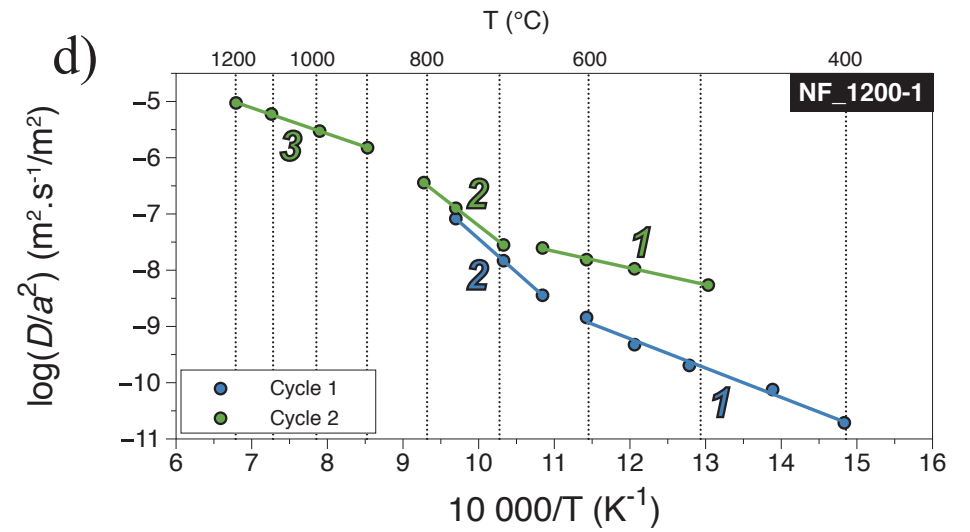
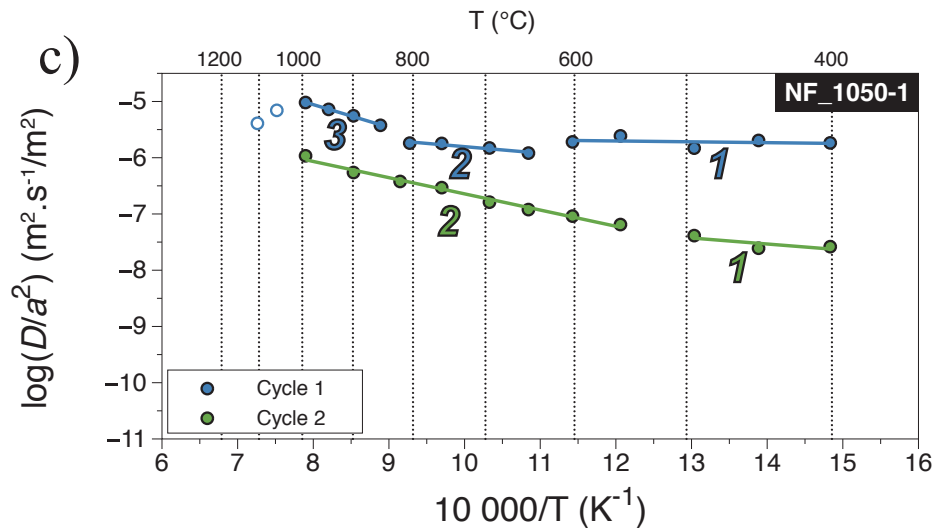
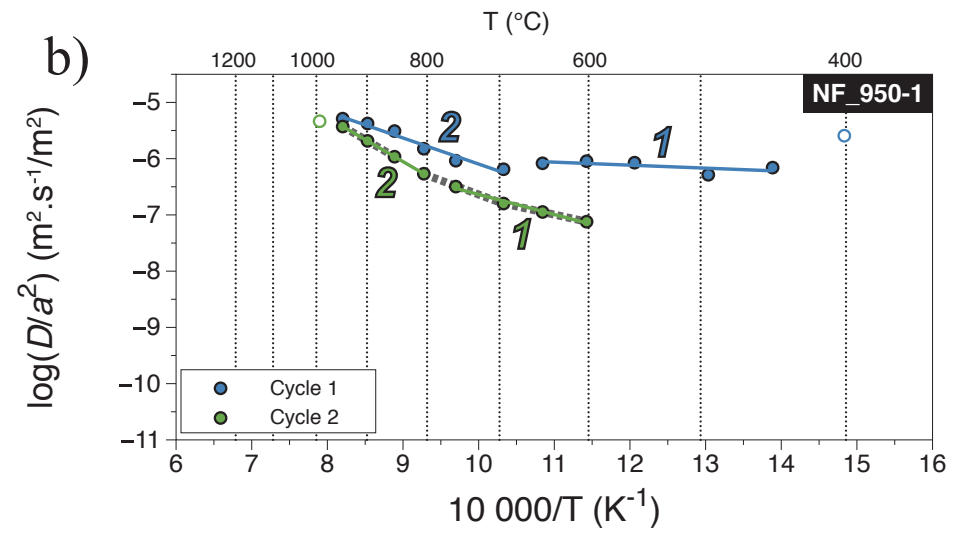
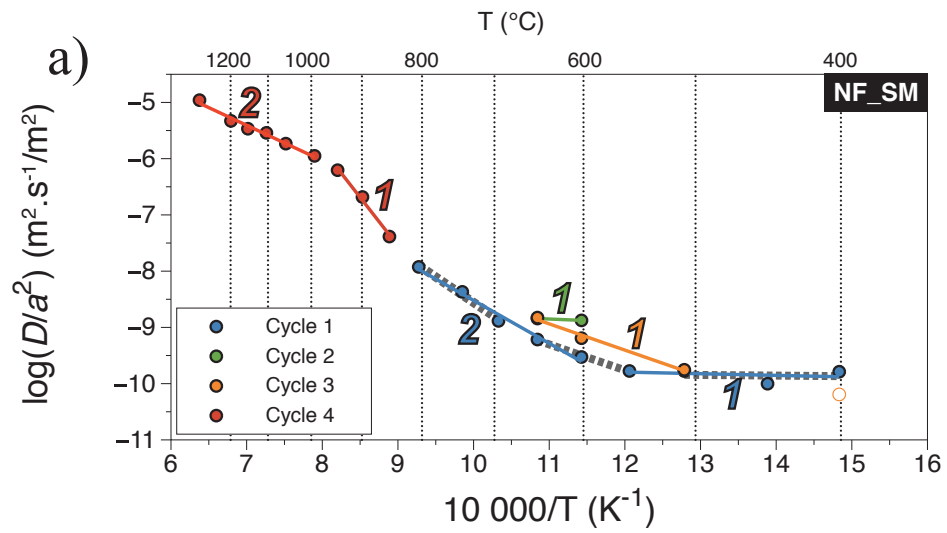


Figure 4

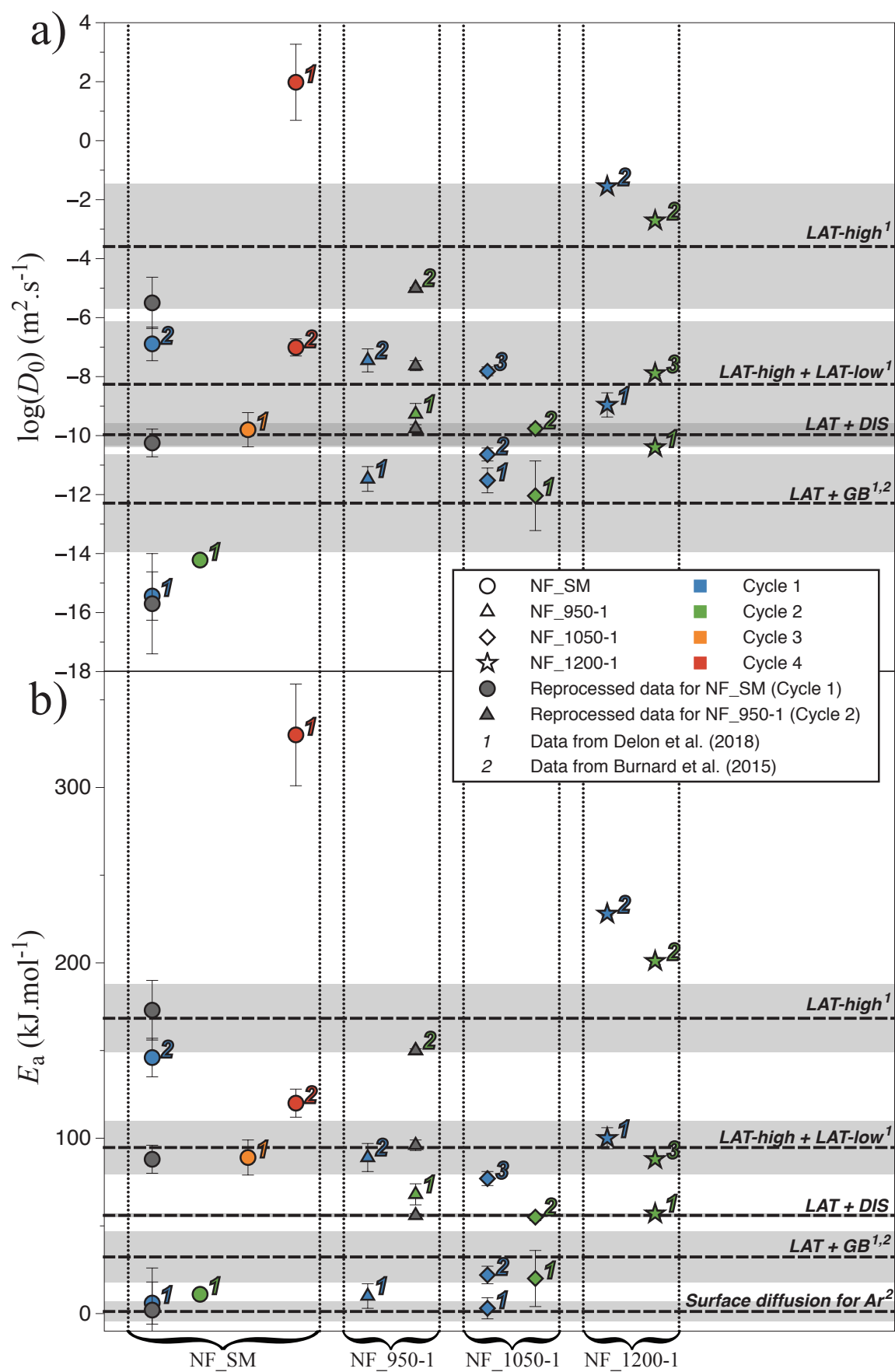


Figure 5

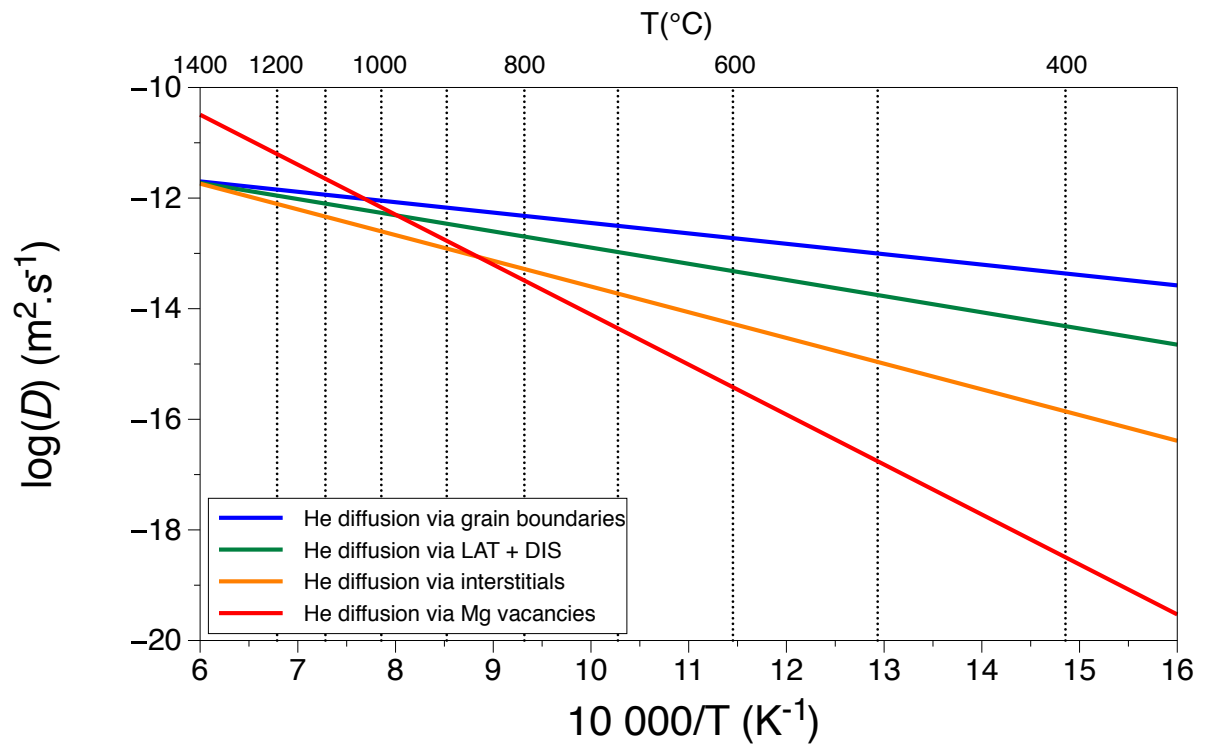


Figure 6

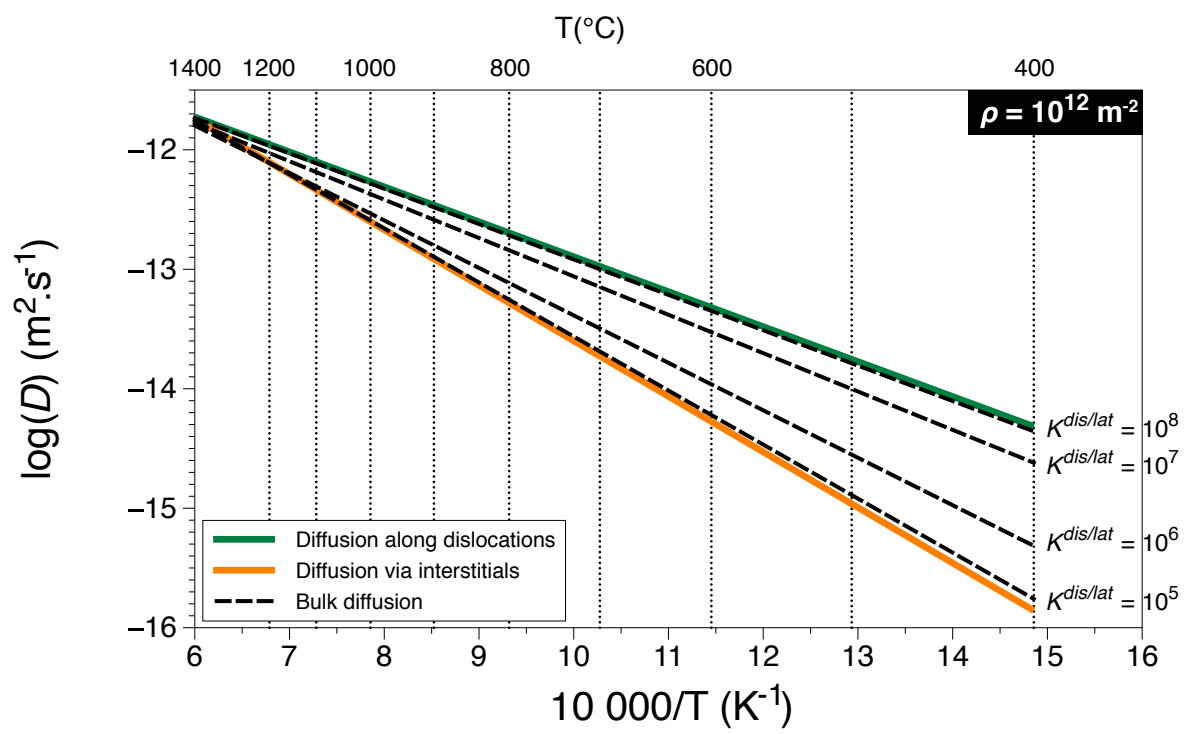


Figure 7